Asian Journal of Chemistry; Vol. 38, No. 9 (2026), 2463-2480
ASIAN JOURNAL OF CHEMISTRY
https://doi.org/10.14233/ajchem.2026.36450

One-Pot Hydrothermal Synthesis of $NiFe_2O_4$ Immobilized on Reduced Graphene Oxide: Characterization and Photocatalytic Application for Environmental Remediation

SNEHAL V. DARANADALE[1], RUPALI D. MURADE[1], AMIT S. WAGHMARE[2], DINESH P. HASE[3] and VAISHALI D. MURADE[1,*]

[1]Department of Chemistry, Padmashri Vikhe Patil College of Arts, Science and Commerce (Affiliated to Savitribai Phule Pune University, Pune) Pravaranagar, Loni KD-413713, India
[2]Department of Chemistry, Arts, Commerce and Science College, (Affiliated with Savitribai Phule Pune University, Pune), Satral-413711, India
[3]Department of Pharmacognosy, Amrutvahini College of Pharmacy (Autonomous), Sangamner-422608, India

*Corresponding author: E-mail: vaishali.hase66@gmail.com

Received: 27 May 2026 *Accepted*: 19 August 2026 *Published online*: 5 September 2026 AJC-22475

Wastewater generated by the textile industry contains substantial amounts of organic pollutants, particularly synthetic dyes, which pose serious risks to human health and aquatic ecosystems. The removal of these contaminants from water bodies is essential, necessitating the development of cost-effective and efficient treatment strategies. The present study focuses on the development of cost-effective nanostructured materials for dye removal from wastewater and antibacterial activity against both Gram-positive and Gram-negative bacteria. A $NiFe_2O_4$/rGO heterojunction was synthesized *via* a one-pot hydrothermal method and characterized to assess its structure, morphology and optical properties. The synthesized material was evaluated for its catalytic removal of methylene blue (MB) and malachite green (MG) dyes and $NiFe_2O_4$/rGO (10%) showed 98.01% and 98.53% removal of MB and MG dyes, respectively, in 120 min. The catalytic removal rate of $NiFe_2O_4$/rGO (10%) heterojunction was much faster (98.01%; 98.53%) than the pure $NiFe_2O_4$ (73.43%; 73.16%) under visible light illumination. The substantial stability and reusability of the heterojunction were assessed through repeated photocatalytic degradation cycles. Its antibacterial activity was evaluated against the selected multidrug-resistant microorganisms, with $NiFe_2O_4$/rGO exhibiting significant zones of inhibition against both bacterial strains. These findings support the potential application of $NiFe_2O_4$/rGO in wastewater treatment, particularly for the removal of organic dyes and bacterial contaminants.

Keywords: Nickel ferrite, Reduced graphene oxide, Malachite green, Methylene blue, Photocatalytic removal, Antibacterial activity.

INTRODUCTION

Over the past few decades, rapid industrialization has both benefited and plagued humanity. Organic pollutants, heavy metals and antibiotics released from textile, dyeing, pharmaceutical industries contaminate water resources and pose serious threats to aquatic life and ecological balance. The growing environmental concerns associated with rapid industrialization have increased the need for effective strategies to protect and restore water quality [1-4]. Therefore, today, water purification has become a crucial responsibility to combat the uncontrollable and irreversible damage caused by the pollutants [5,6]. Dyes are used as a raw material, particularly in the food, printing, paper, paint, cosmetic and textile industries. Many synthetic dyes are toxic, carcinogenic and resistant to biodegradation. Their presence in contaminated water can pose both immediate and long-term health risks to humans and other living organisms [7-10]. Cationic dyes such as methylene blue (MB) and malachite green (MG) cause mutagenic malignancies and reproductive disorders in living organisms [11-14]. Therefore, treating industrial effluents before releasing them into water streams is a prime concern today.

Photocatalysis based on semiconductor materials is a promising approach for treating contaminated water and reducing environmental pollution. Magnetic spinel ferrites (MFe_2O_4; M = Ni, Co, Mn, Zn, Cu, Ca, *etc.*) possess semiconductor properties and have been investigated for applications such as gas sensing [15], photocatalysis [16,17], CO_2 reduction

[18,19] and hydrogen production [20]. Their chemical and mechanical stability, high electrical resistivity and magnetic separability make them attractive for environmental applications [21,22]. Despite these advantages, pristine spinel ferrites generally exhibit limited photocatalytic activity. $NiFe_2O_4$, with a narrow band gap of approximately 1.7 eV, can suffer from rapid recombination of photogenerated electron-hole pairs, which limits its photocatalytic efficiency. Coupling $NiFe_2O_4$ with another semiconductor to form a magnetically recoverable heterojunction can improve charge separation and enhance photocatalytic performance, making this approach suitable for wastewater treatment.

Reduced graphene oxide (rGO) is a 2D sp^2-hybridized carbon material with high surface area, electrical conductivity and electron mobility, making it useful for photocatalytic applications. Its conductive network facilitates the separation and transport of photoexcited charge carriers, while its abundant surface sites promote dye adsorption through π-π interactions, hydrogen bonding and electrostatic interactions [23-28]. Incorporation of rGO with spinel ferrites such as $NiFe_2O_4$ can suppress electron-hole recombination at the heterojunction interface and provide additional active sites, thereby improving photocatalytic activity [29,30]. Previous studies have reported the use of ferrite/rGO composites for the degradation of organic pollutants [31,32]. Based on these properties, rGO was integrated with $NiFe_2O_4$ in the present study to serve as an electron mediator, facilitate charge transfer and enhance the photocatalytic degradation of dye pollutants [33-35].

Several challenges remain in improving the photocatalytic activity and efficiency of these materials. In this study, the $NiFe_2O_4$/rGO heterojunction was prepared by a simple hydrothermal method. The optical, textural, structural and surface properties of pristine $NiFe_2O_4$ and the $NiFe_2O_4$/rGO heterojunction were studied using different characterization techniques. The photocatalytic activity was evaluated using methylene blue (MB) and malachite green (MG) as model dye pollutants.

EXPERIMENTAL

All reagents were of analytical grade and used without further purification. Ferrous ammonium sulphate hexahydrate ($(NH_4)_2Fe(SO_4)_2\cdot 6H_2O$, 99%), nickel chloride hexahydrate ($NiCl_2\cdot 6H_2O$, 98%), polyethylene glycol (PEG-600), sodium hydroxide (97%), hydrazine hydrate, disodium salt of ethylenediamine-tetraacetic acid (EDTA-2Na, 99.5%), benzoquinone (BQ, 98%), isopropyl alcohol (IPA, 98%), methylene blue (MB) and malachite green (MG) were procured from Merck and Loba Chemie Pvt. Ltd. India. Reduced graphene oxide (rGO) was obtained from Techinstro Industries, India. The deionized (DI) water was employed for all experiments.

One-pot hydrothermal synthesis of $NiFe_2O_4$/rGO heterojunction: For the synthesis of the $NiFe_2O_4$/rGO hetero-junction, $(NH_4)_2Fe(SO_4)_2\cdot 6H_2O$ (3.33 g) and $NiCl_2\cdot 6H_2O$ (1.01 g) were dissolved in 50 mL of deionized water and stirred until a homogeneous solution was obtained. Subsequently, 40 mL of PEG-600 was added dropwise to the solution at 45 ºC under continuous stirring to obtain a clear solution (solution I). Separately, 1 mL of hydrazine hydrate and 4 g of NaOH were dissolved in 10 mL of deionized water and stirred for 1 h (solution II). Solution II was added dropwise to solution I, followed by ultrasonication for 30 min. The required amount of rGO (0.0935 g for 10 wt.%) was then added to the mixture and stirred at room temperature for 1 h. The resulting suspension was transferred to a Teflon-lined autoclave and heated at 180 ºC for 8 h. The resulting precipitate was washed repeatedly with deionized water (1.5 L) and ethanol (500 mL), followed by drying at 80 ºC overnight. The dried material was designated as $NiFe_2O_4$/rGO (10%). $NiFe_2O_4$/rGO heterojunctions containing 5 and 15 wt.% rGO were prepared under the same conditions by varying the amount of rGO accordingly [36].

Characterization: In order to ascertain the crystallinity and phases present in the synthesized samples, a comprehensive X-ray diffraction analysis was conducted utilizing a Bruker AXS D8 Focus X-ray diffractometer equipped with a Cu*K*α radiation source (λ = 1.540 Å). An energy dispersive spectrometer (EDS) (Ametek, Octane Plus model) was utilized alongside a field emission scanning electron microscope (FE-SEM) known as Nova NanoSEM 450 FEI and a high-resolution transmission electron microscope (HR-TEM) model JEM-F200 (URP) operating at 10 kV. This combination was employed to analyze the elemental composition, structural and textural properties of the heterojunction. In order to conduct a thorough analysis of the oxidation states and elemental compositions of the $NiFe_2O_4$/rGO heterojunction, X-ray photoelectron spectroscopy was employed. Spectroscopic investigations were conducted utilizing the Physical Electronics, PHI 5000 Versa Probe III instrument. The UV-visible spectrophotometer (UV-Vis 2600) was utilized to acquire UV-visible DRS spectra. Through a detailed analysis of the nitrogen adsorption-desorption curve obtained from the nitrogen adsorption analyzer (Quantachrome NovaWin), the surface areas of the samples were systematically evaluated. The electrochemical impedance spectroscopy (EIS) was carried out using an electrochemical workstation Metrohm model (Netherland). For photoluminescence (PL) analysis was carried out using Jasco spectrofluorometer Model FP-8300 WRE using 350 nm as the excitation wavelength. Total organic carbon (TOC) was measured using an Enviro TOC analyzer (Elementar, Germany). UV-Visible absorption spectra were recorded using a Shimadzu UV-1800 UV-Visible spectrophotometer, with deionized water used as the reference.

Photocatalytic degradation study: The photocatalytic degradation performance of pristine $NiFe_2O_4$ and $NiFe_2O_4$/rGO heterojunction was evaluated according to a previously reported method [37]. Briefly, 30 mg of photocatalyst was dispersed in 10 mg/L dye solution and stirred continuously in the dark for 30 min to establish adsorption-desorption equilibrium. The suspension was then irradiated with a 300 W xenon lamp to initiate the photocatalytic reaction. At 10 min intervals, 5 mL of the reaction mixture was withdrawn, centrifuged and analyzed by UV-Visible spectrophotometry at 617 nm. The dye concentration at time 't' and the photocatalytic degradation efficiency were calculated using the following equations:

$$\text{Concentration} = \frac{A_t}{A_o} \times C_o \times 100 \quad (1)$$

$$\text{Degradation efficiency (\%)} = \frac{C_o - C_t}{C_o} \times 100 \qquad (2)$$

where A_t, A_o, are the absorbance at time t and at time zero and C_o and C_t are the concentrations at time zero and at time t, respectively.

Antimicrobial activity: The antibacterial activity of synthesized $NiFe_2O_4$ NPs and $NiFe_2O_4$/rGO NCs was evaluated using the well diffusion method with multiple drug-resistant bacteria, namely Gram-positive *S. aureus* (NCIM 2654) and Gram-negative *E. coli* (NCIM 2256), at a concentration of 2 mg/mL. The resulting suspensions of bacteria were diluted to a final absorbance of 0.02 at 600 nm using a UV-visible spectrophotometer (Shimadzu-1900i), *i.e.* 2×10^7 CFU. All preparation and operations were performed under aseptic conditions; wells were shaped on the sterile nutrient agar plate and 50 µL sample was added into each well. The antibacterial activity was assessed by calculating the diameter of zones of inhibition after incubation at 37 ºC for 24 h [38-40].

Determination of minimum inhibitory concentration (MIC): The MIC of $NiFe_2O_4$ NPs and $NiFe_2O_4$/rGO heterojunction was determined using a modified broth microdilution method [39,41]. Two-fold serial dilutions of $NiFe_2O_4$ and $NiFe_2O_4$/rGO, ranging from 12.5 to 400 mg/mL, were prepared in Mueller-Hinton broth using 96-well microtiter plates. Equal volumes (100 µL) of each nanoparticle dilution and bacterial suspension adjusted to 0.5 McFarland standard (approximately 1×10^8 CFU/mL) were added to the respective wells. The plates were incubated at 37 ºC for 24 h. A negative control containing the nanoparticle suspension and culture medium and a positive control containing the bacterial suspension and culture medium, were maintained under the same conditions. After incubation, 100 µL from each well was transferred onto Mueller-Hinton agar plates and incubated at 37 ºC for 24 h.

RESULTS AND DISCUSSION

Powder XRD studies: X-ray diffraction (XRD) analysis was performed to identify the crystalline phases of the synthesized materials and the corresponding patterns are shown in Fig. 1. The diffraction peaks at 2θ = 30.01º, 35.36º, 36.99º, 42.99º, 44.14º, 53.35º, 56.87º, 62.45º, 70.86º, 73.90º, 74.91º and 78.87º correspond to the crystallographic planes (2 2 0), (3 1 1), (2 2 2), (4 0 0), (3 3 1), (4 2 2), (5 1 1), (4 4 0), (6 2 0), (5 3 3), (6 2 2) and (4 4 4), respectively. These reflections are consistent with the cubic nickel ferrite phase (JCPDS No. 10-0325) [36,42]. The characteristic peak at 26.5º is attributed to the (002) plane of rGO [23,43]. The incorporation of rGO results in a decrease in the intensity of the $NiFe_2O_4$ diffraction peaks, indicating a reduction in the apparent crystallinity of the $NiFe_2O_4$ phase within the $NiFe_2O_4$/rGO heterojunction.

The crystalline size of $NiFe_2O_4$ and $NiFe_2O_4$/rGO heterojunction was calculated from the Debye-Scherrer equation:

$$\Phi = \frac{0.9\lambda}{\beta \cos\theta}$$

The calculated crystallite sizes of $NiFe_2O_4$ and $NiFe_2O_4$/rGO (10%) were found to be 73.34 nm and 56.13 nm for pure $NiFe_2O_4$ and $NiFe_2O_4$/rGO (10%) heterojunction, respectively.

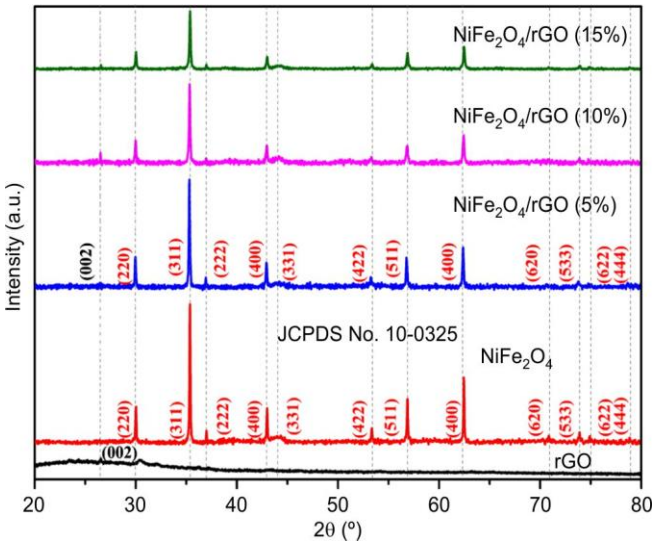

Fig. 1. XRD spectra of rGO, pure $NiFe_2O_4$, $NiFe_2O_4$/rGO (5%), $NiFe_2O_4$/rGO (10%) and $NiFe_2O_4$/rGO (15%) heterojunctions

Morphological studies: FESEM analysis was carried out to examine the surface morphology of pristine $NiFe_2O_4$ and the $NiFe_2O_4$/rGO (10%) heterojunction. The corresponding micrographs are shown in Fig. 2. The FESEM images of $NiFe_2O_4$ (Fig. 2a-c) show octahedral- and hexagonal-like particles with some degree of agglomeration. Such agglomeration may arise from magnetic and van der Waals interactions between the nanoparticles [44,45]. Small, irregularly shaped nickel ferrite nanospheres are visible in the micrographs. In the $NiFe_2O_4$/rGO (10%) heterojunction (Fig. 2d-f), $NiFe_2O_4$ NPs are distributed over the rGO surface. The aggregation of $NiFe_2O_4$ NPs is reduced in the $NiFe_2O_4$/rGO heterojunction, indicating that rGO provides a supporting surface that limits nanoparticle agglomeration.

EDX spectroscopy was used to determine the elemental composition of the prepared materials and the results are shown in Fig. 3. The EDX spectra of the $NiFe_2O_4$/rGO (10%) heterojunction (Fig. 3a-b) contain signals corresponding to Ni, Fe, C and O. No additional elemental signals were detected, supporting the purity of the prepared material. Elemental mapping of $NiFe_2O_4$ (Fig. 3c-e) and $NiFe_2O_4$/rGO (10%) (Fig. 3f-i) further confirms the distribution of the constituent elements. The mapping images of the heterojunction indicate a uniform distribution of $NiFe_2O_4$ nanoparticles over the rGO surface.

TEM, HRTEM and SAED analyses were performed to further examine the morphology and crystalline structure of the samples (Fig. 4). The TEM images of pristine $NiFe_2O_4$ (Fig. 4a-b) reveal aggregated nanoparticles. The lattice spacing of 0.247 nm observed in the HRTEM image (Fig. 4c) corresponds to the (311) plane of $NiFe_2O_4$. The TEM images of $NiFe_2O_4$/rGO (10%) (Fig. 4d-f) show $NiFe_2O_4$ nanoparticles distributed across the relatively transparent rGO sheets. A lattice spacing of 0.206 nm, observed in Fig. 4g, can be assigned to the (400) plane of $NiFe_2O_4$. The incorporation of $NiFe_2O_4$ onto rGO improves nanoparticle dispersion and limits particle aggregation, while providing additional interfacial sites [46]. The SAED pattern of pristine $NiFe_2O_4$ (Fig. 4h) shows distinct diffraction rings corresponding to the (220), (311), (400),

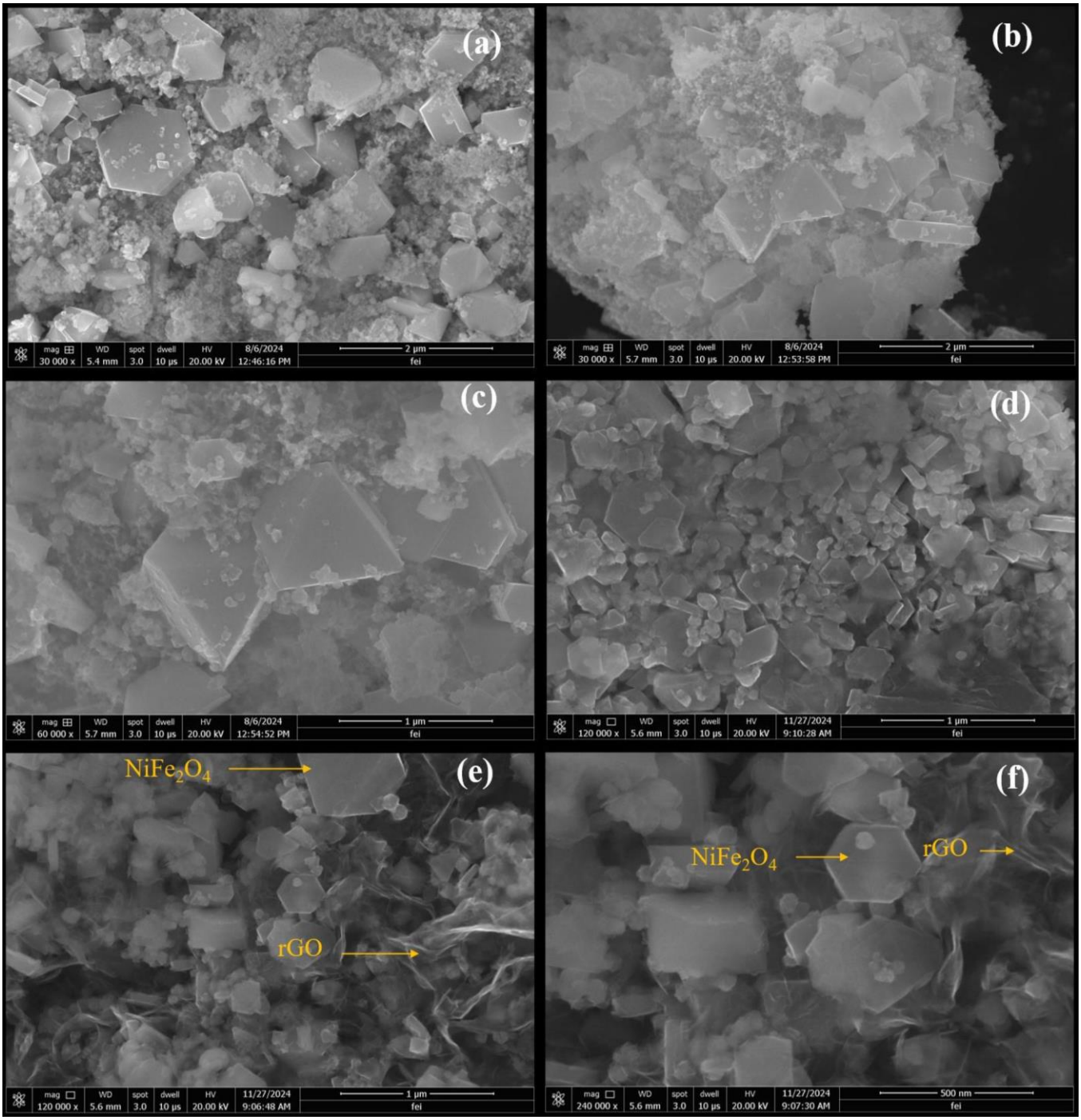

Fig. 2. FE-SEM micrographs of $NiFe_2O_4$ (a-c) and $NiFe_2O_4$/rGO (10%) heterojunction (d-f)

(533), (620) and (444) planes, confirming its crystalline structure [47,48]. The $NiFe_2O_4$/rGO (10%) heterojunction (Fig. 4i) exhibits characteristic diffraction rings, confirming its polycrystalline nature.

XPS studies: The XPS study was performed to explore the chemical composition and element valence states of the synthesized samples. The survey scan (Fig. 5a) of $NiFe_2O_4$/rGO (10%) heterojunction exhibits the characteristic peaks of nickel (2*p*), iron (2 *p*), carbon (1*s*) and oxygen (1*s*) species. Four peaks can be seen in the Ni 2*p* deconvolution spectrum, as shown in Fig. 5b. Two shake-up satellite peaks are present at binding energies 861.84 eV and 872.44 eV. The satellite peak of Ni 2*p* at 861.84 eV confirmed the +2 oxidation state of nickel in the $NiFe_2O_4$/rGO (10%). The peaks at 855.79 eV and 873.89 eV are assigned to Ni $2p_{3/2}$ and Ni $2p_{1/2}$, respectively. These results align well with the literature findings [49]. The deconvoluted spectrum of Fe 2*p* (Fig. 5c) exhibited two prominent peaks at 713.98 eV and 724.78 eV that correspond to Fe $2p_{3/2}$ and Fe $2p_{1/2}$, respectively. A satellite peak for Fe $2p_{3/2}$ at 718.98 eV further validated the presence of the +3 oxidation state of iron in $NiFe_2O_4$/rGO (10%) [1]. Two peaks at 283.34 eV and 285.74 eV, which correspond to the C=C

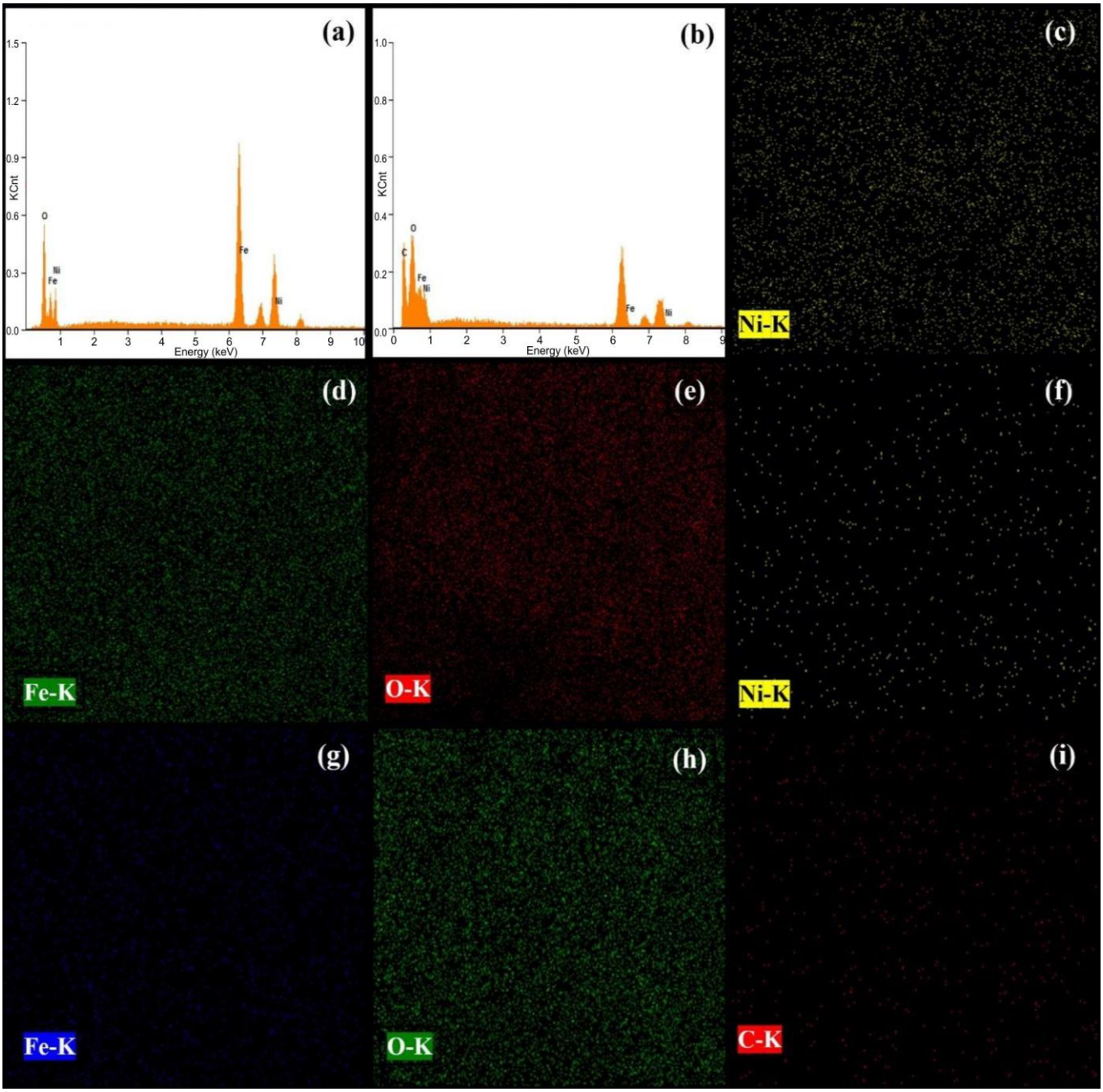

Fig. 3. EDX spectra of $NiFe_2O_4$ (a) and $NiFe_2O_4$/rGO (10%) (b) and elemental mapping spectra of $NiFe_2O_4$ (c-e) and $NiFe_2O_4$/rGO (f-i)

bond of alkene and C=O bonds of aromatic rings in the rGO (Fig. 5d) [50,51]. In the 1*s* spectrum of oxygen, a peak at 531.24 eV is attributed to the lattice oxygen in the Ni/Fe-O framework (Fig. 5e) [52]. All of these findings confirmed that the $NiFe_2O_4$/rGO (10%) heterojunction was successfully synthesized.

UV-Visible DRS and PL studies: UV-Visible diffuse reflectance spectroscopy (DRS) was used to study the optical properties of the synthesized materials and the corresponding spectra are shown in Fig. 6. Pristine $NiFe_2O_4$ shows relatively weak absorption in the visible region, whereas the $NiFe_2O_4$/rGO (10%) heterojunction exhibits stronger visible-light absorption. Increasing the rGO content enhances light absorption and shifts the absorption edge toward longer wavelengths [23,53]. This improved optical response can be attributed to the interaction between $NiFe_2O_4$ and rGO. The optical band gap energy (E_g) was estimated using the Tauc equation [23]. The inset plots in Fig. 6a-b give band gap values of 1.49 eV for $NiFe_2O_4$ and 1.34 eV for $NiFe_2O_4$/rGO (10%), based on a direct allowed transition.

Photoluminescence (PL) spectroscopy was used to assess the recombination of photogenerated charge carriers (Fig. 6c). The $NiFe_2O_4$/rGO (10%) heterojunction exhibits lower PL intensity than pristine $NiFe_2O_4$, which reflects suppressed electron-hole recombination and longer-lived photogenerated charge carriers [54]. The improved charge separation contri-

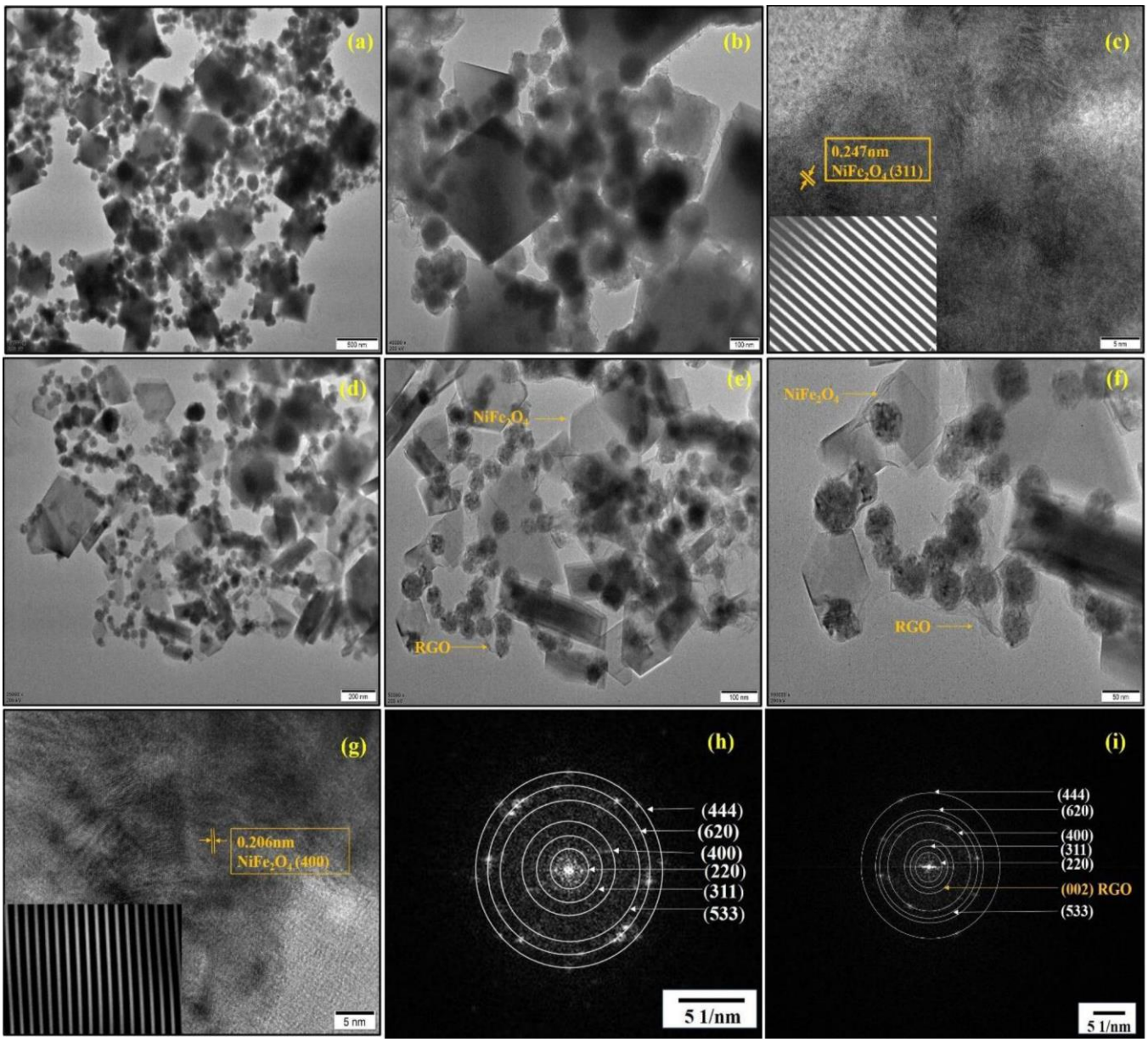

Fig. 4. TEM micrographs (a-b), HR-TEM (c) of $NiFe_2O_4$ and TEM micrographs (d-f) and HR-TEM (g) of $NiFe_2O_4$/rGO (10%) heterojunction and SAED pattern of $NiFe_2O_4$ (h) and $NiFe_2O_4$/rGO (10%), (i) heterojunction

butes to the higher photocatalytic activity of the $NiFe_2O_4$/rGO (10%) heterojunction.

Electrochemical impedance analysis: Electrochemical impedance spectroscopy (EIS) was performed to study charge transfer and separation in the synthesized materials [55]. A larger impedance arc generally reflects greater resistance to charge transfer [56]. As shown in Fig. 7a, the $NiFe_2O_4$/rGO (10%) heterojunction exhibits a smaller impedance arc than pristine $NiFe_2O_4$, corresponding to lower charge-transfer resistance and more efficient charge transport. The improved charge-transfer behaviour can be attributed to the interaction between the conductive rGO sheets and $NiFe_2O_4$, which facilitates the movement of photogenerated charge carriers and improves photocatalytic performance.

Nitrogen adsorption/desorption isotherm: The N_2 adsorption/desorption isotherm measurement was employed to determine the BET surface area of the pure nickel ferrite and $NiFe_2O_4$/rGO (10%) heterojunction. The N_2 adsorption/desorption isotherm shows a type IV hysteresis loop, which confirmed the mesoporous characteristics of the nanocomposites. The measured BET surface areas for pure $NiFe_2O_4$ and $NiFe_2O_4$/rGO (10%) heterojunction are 21.184 m^2 g^{-1} and 31.003 m^2 g^{-1}, respectively. The $NiFe_2O_4$/rGO (10%) heterojunction has a higher BET surface area than pristine $NiFe_2O_4$, providing more sites for dye adsorption. The larger surface area facilitates contact between the photocatalyst and MB or MG molecules, which can improve their photocatalytic degradation [2]. The pore size distribution curves calculated by the Barrett-Joyner-Halenda (BJH) method are shown in Fig. 7c. Compared with pristine $NiFe_2O_4$, the $NiFe_2O_4$/rGO (10%) heterojunction has a higher surface area and pore volume, along with a smaller pore size (Table-1). These textural prop-

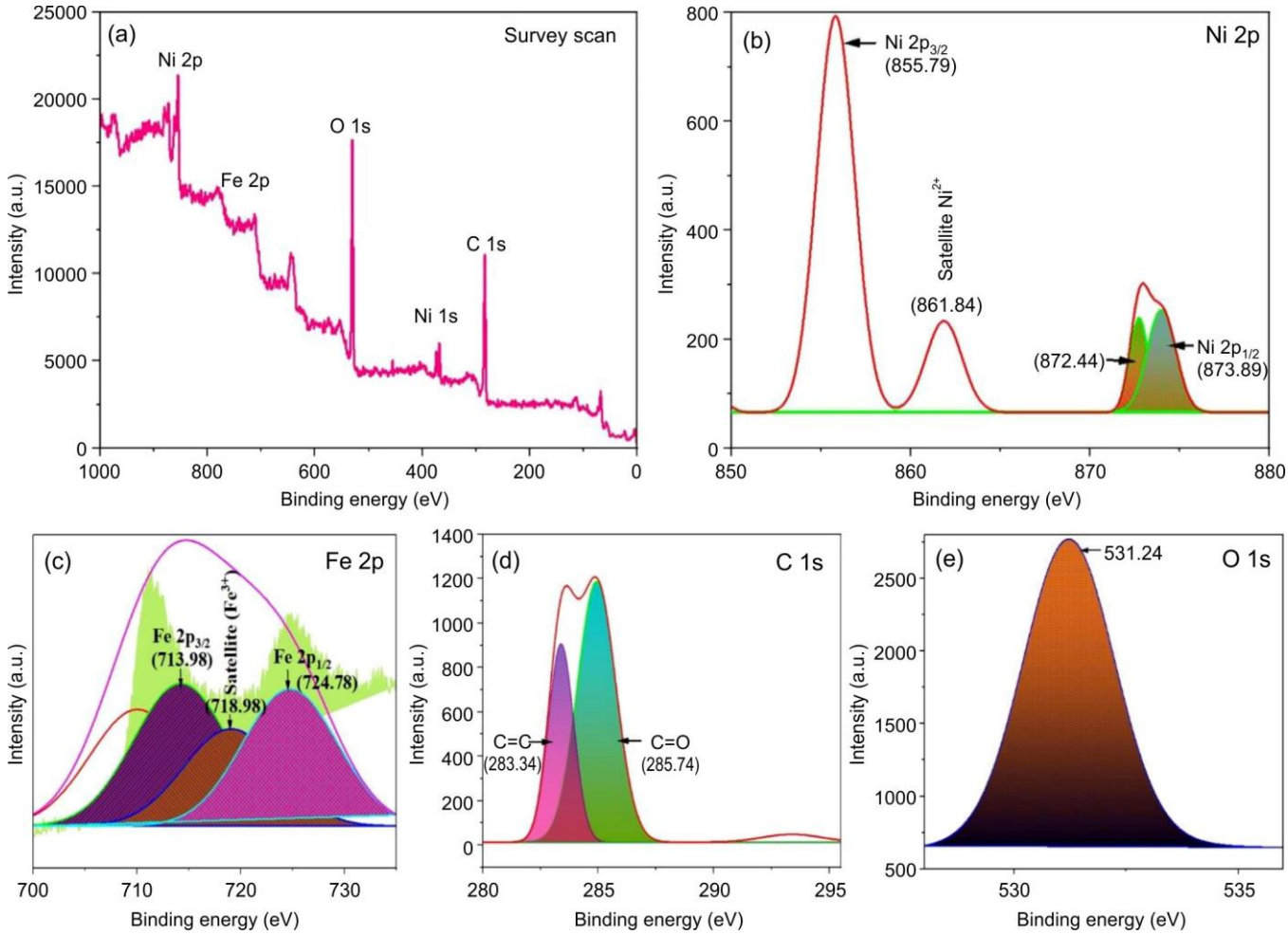

Fig. 5. XPS spectra of $NiFe_2O_4$/rGO (10%) heterojunction; survey scan (a), Ni 2p (b), Fe 2p (c), C 1s (d) and O 1s (e)

TABLE-1
SURFACE AREA, PORE VOLUME AND AVERAGE PORE SIZE OF PURE $NiFe_2O_4$ AND $NiFe_2O_4$/rGO (10%)

Sample	S_{BET} (m^2/g)	Pore volume (cc/g)	Average pore size (nm)
$NiFe_2O_4$	21.184	0.024	3.09
$NiFe_2O_4$/rGO (10%)	31.003	0.039	2.73

erties provide more accessible surface sites for dye molecules and can improve the photocatalytic degradation of MB and MG dyes.

Photocatalytic degradation: The catalytic efficacy of the synthesized photocatalyst was examined using MB and MG dyes as test pollutants and the results are displayed in Fig. 8a-b. Pure nickel ferrite had a restricted ability to degrade MB (73.43%) and MG (73.16%). However, the degradation of MB (98.01%) and MG (98.53%) was significantly improved by the $NiFe_2O_4$/rGO (10%) heterojunction. Increasing the rGO content led to a gradual improvement in the degradation capacity of the heterojunction. Within 120 min, the 10% $NiFe_2O_4$/rGO photocatalyst had an excellent degrading efficacy for MB (98.01%) and MG (98.53%). The increased photocatalytic efficacy of the $NiFe_2O_4$/rGO (10%) photocatalyst could be due to the utilization of complete solar light of the electromagnetic spectrum and the enhanced the separation photoexcited e^-/h^+ pairs during the photocatalysis reaction. This could be due to the united effect of rGO and nickel ferrite nanoparticles [57, 58].

Furthermore, the photodegradation of MB and MG dyes followed pseudo first-order kinetics, depicted in Fig. 9a-b. After exposure of MB containing samples to light in the absence of a catalyst (photolysis), rGO, $NiFe_2O_4$/rGO (5%), $NiFe_2O_4$/rGO (10%) and $NiFe_2O_4$/rGO (15%) as catalysts exhibit rate constants of 0.0009 min^{-1}, 0.0019 min^{-1}, 0.0093 min^{-1}, 0.0245 min^{-1} and 0.0168 min^{-1} respectively. Similarly, for MG, the rate constants were computed as 0.0040 min^{-1}, 0.0103 min^{-1}, 0.0123 min^{-1}, 0.0219 min^{-1}, 0.0144 min^{-1}, respectively. It was observed that the rate constant (k) of the $NiFe_2O_4$/rGO (10%) heterojunction (0.0245 min^{-1}) is approximately 2.63 higher than pure $NiFe_2O_4$ (0.0093 min^{-1}) towards MB. Similarly, the rate constant (k) of the $NiFe_2O_4$/rGO (10%) heterojunction (0.0219 min^{-1}) is approximately 2.13 higher than pure $NiFe_2O_4$ (0.0103 min^{-1}) towards the MG dye.

Effect of catalyst concentration: Fig. 8c-d illustrate the effect of the $NiFe_2O_4$/rGO (10%) catalyst dose on the photodegradation of MB and MG dyes. As the concentration of the photocatalyst rose, the photocatalytic efficacy also increased, as observed in Fig. 9c-d. When the catalyst dose was increased from 15 mg to 30 mg, the photocatalytic degradation

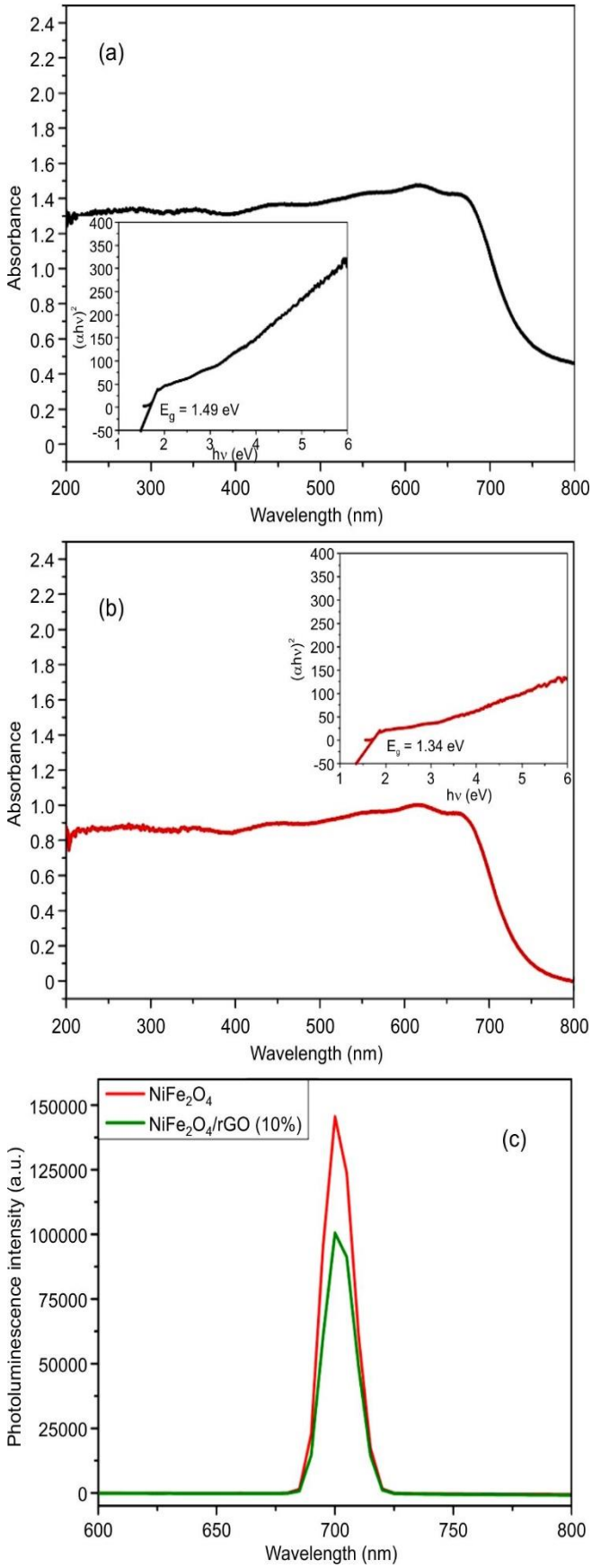

Fig. 6. UV-visible DRS spectra and their Tauc plots (insets) of pure $NiFe_2O_4$ (a), $NiFe_2O_4$/rGO (10%) heterojunction (b) and PL analysis (c) of $NiFe_2O_4$ and $NiFe_2O_4$/rGO (10%)

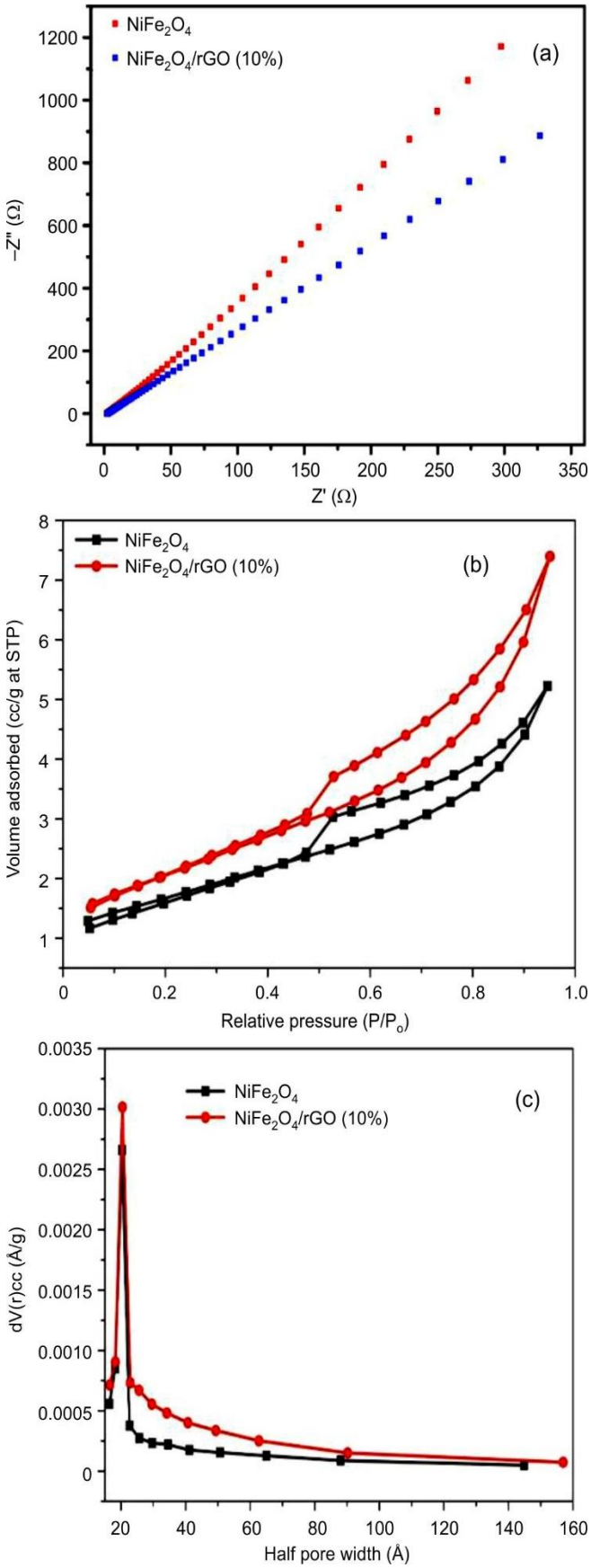

Fig. 7. Nyquist plot (EIS) of the prepared photocatalysts (a), the isothermal adsorption/desorption curves of N_2 (b) and the pore size distribution curves (c) of $NiFe_2O_4$ and $NiFe_2O_4$/rGO (10%) heterojunction

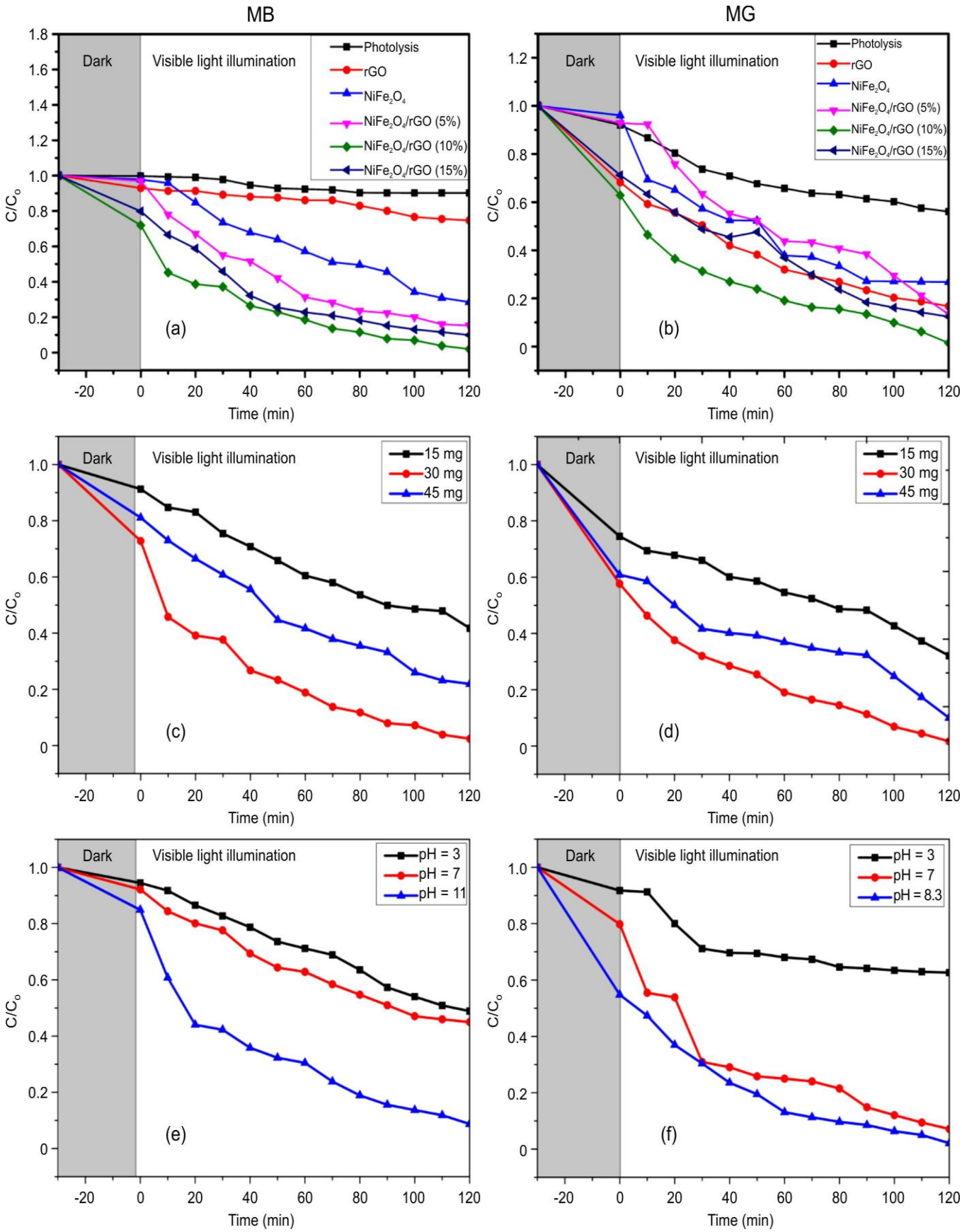

Fig. 8. Photocatalytic degradation of MB and MG dyes: (a,b) using as-prepared photocatalysts, (c,d) using different concentrations of $NiFe_2O_4$/rGO (10%) heterojunction and (e,f) at different pH conditions using $NiFe_2O_4$/rGO (10%) heterojunction

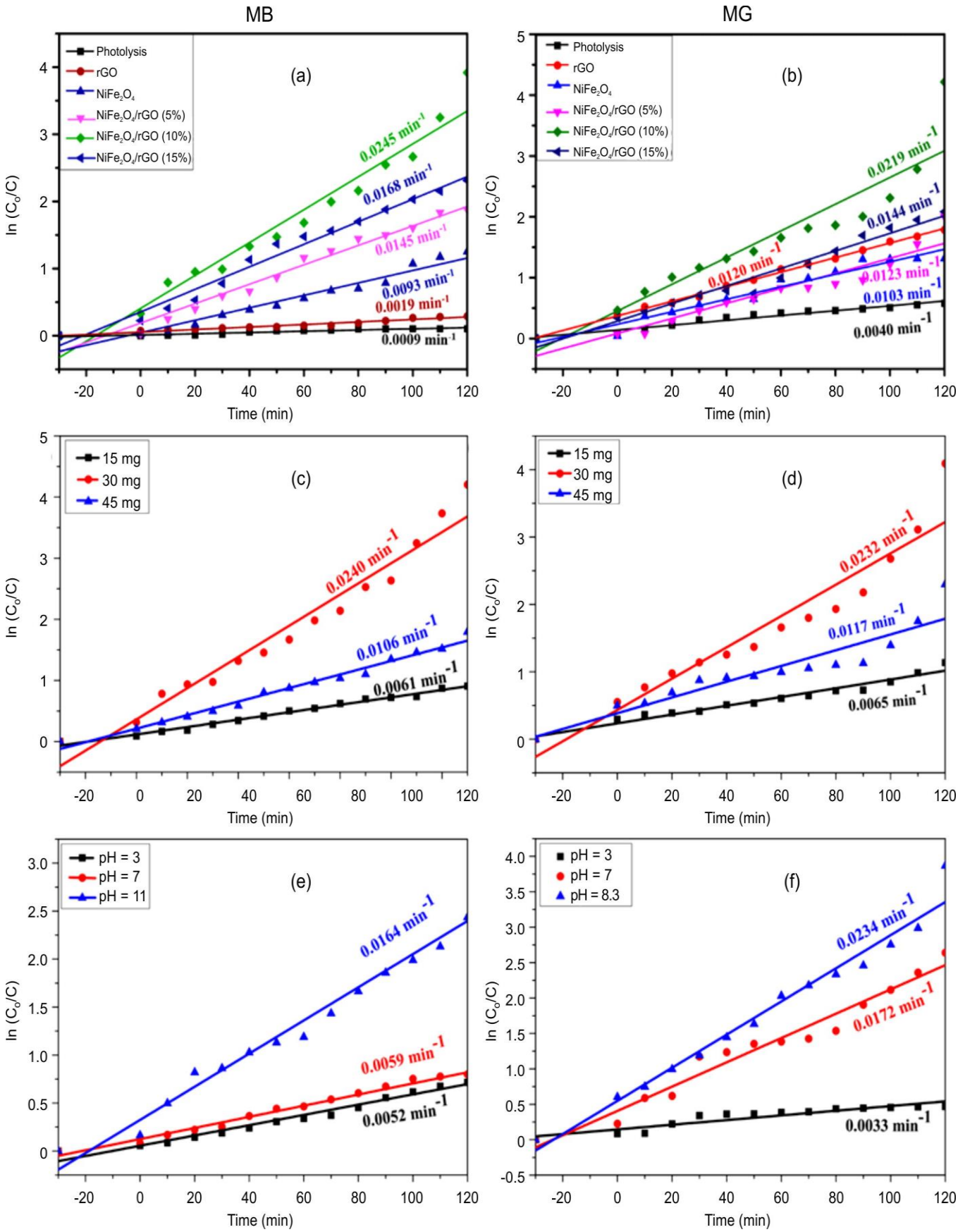

Fig. 9. Photocatalytic degradation of MB using different concentrations and pH using the $NiFe_2O_4$/rGO (10%) catalyst (a and d) and pseudo-first-order kinetic plots of ln (C_o/C) *vs.* time (c and f)

ability rose from 58.27% to 97.61% and from 67.90% to 98.33% for MB and MG dyes, respectively. This significant improvement might be the result of enhanced catalyst surface active sites, which directly raised the catalytic degradation of MB and MG dyes. Furthermore, Fig. 10a-b show a marked decrease in photodegradation efficiency when the catalyst dosage was increased to 45 mg, with MB degradation decreasing from 97.61% to 78.10% and MG degradation from 98.33% to 89.98%. The lower efficiency at higher catalyst loading can be attributed to increased turbidity of the reaction suspension, which limits the penetration of incident light. Excess catalyst may further promote nanoparticle agglomeration, reducing the available surface area and active sites for dye degradation [59-61].

Furthermore, for 15, 30 and 45 mg of $NiFe_2O_4$/rGO (10%) catalyst, the computed rate constants for MB dye were 0.0061 min^{-1}, 0.0240 min^{-1} and 0.0106 min^{-1}, respectively and the computed rate constants for the MG dye were 0.0065 min^{-1}, 0.0232 min^{-1} and 0.0117 min^{-1}, respectively (Fig. 9c-d). These findings indicate that 30 mg of catalyst is the optimum dose to achieve the maximum degradation of MB and MG dye.

Effect of pH: The photocatalytic degradation ability of the $NiFe_2O_4$/rGO (10%) catalyst towards MB and MG dyes was further studied under different pH conditions (for MB, pH = 3 7 and 11 and for MG, pH = 3 7 and 8.3). The results are shown in Figs. 10e-f. For MB dye, the $NiFe_2O_4$/rGO (10%) photocatalyst achieved its highest degradation efficiency of 91.25% at pH 11. But with MG dye, pH 8.3 achieved the

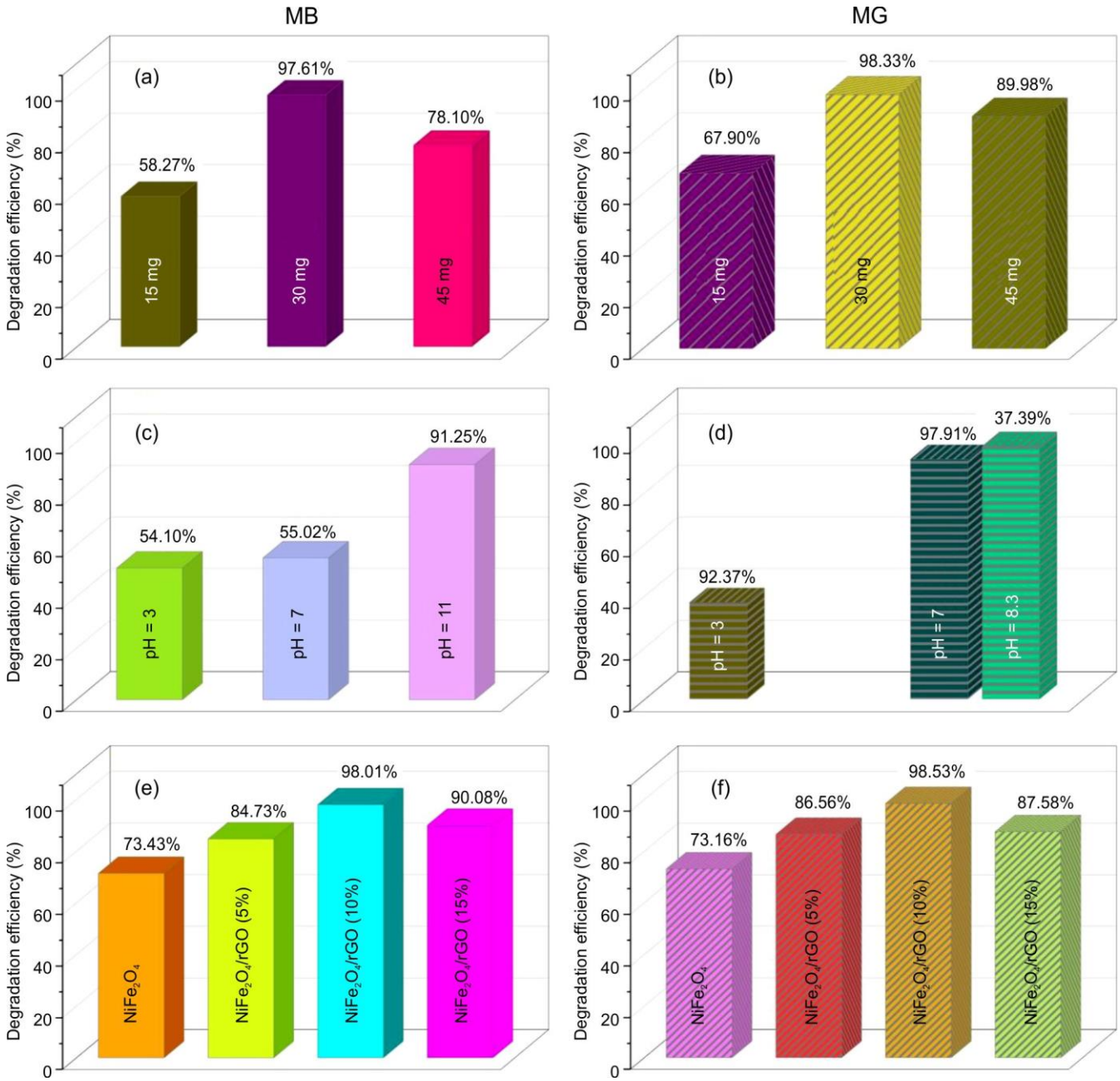

Fig. 10. Degradation efficiency of $NiFe_2O_4$/rGO (10%) catalyst at different dosages (a,b); degradation efficiency of $NiFe_2O_4$/rGO (10%) catalyst at different pH levels (c,d); and degradation efficiency of $NiFe_2O_4$ and $NiFe_2O_4$/rGO (5%, 10%, 15%) catalysts (e,f)

highest degradation efficiency (97.91%) (Fig. 10e-f). Therefore, the optimum pH conditions for the highest degradation of MB and MG dyes, were pH 11 and pH 8.3. This indicates that the adsorption of dye molecules onto the negatively charged surface of the photocatalyst is highly enhanced by the alkaline pH state. The changes in the pH of the solution, thereby, affect the bonding between the photocatalyst and dye molecules as well as the photocatalytic degradation of dye [62,63].

Based on Fig. 9e-f, the observed rate constants for MG dye at pH values (3, 7 and 8.3) are 0.0033 min^{-1}, 0.0172 min^{-1} and 0.0234 min^{-1}, respectively and the computed kinetic rate constants for MB dye at pH values (3, 7 and 11) are 0.0052 min^{-1}, 0.0059 min^{-1} and 0.0164 min^{-1}. At pH 11 and pH 8.3, the highest rate constants of 0.0164 min^{-1} (MB) and 0.0234 min^{-1} (MG) were attained. These findings imply that alkaline conditions promote MB and MG photocatalytic breakdown.

Time-dependent UV-visible spectra for MB and MG dyes: Fig. 11 shows the time-dependent UV-visible absorption spectra of the MB and MG dye solutions at different catalyst dosages and pH. It is evident that the longer the irradiation period, the less dye was absorbed. Furthermore, the colour change of the dye solution shows that, within 120 min of irradiation, the dyes were substantially broken down in the presence of the $NiFe_2O_4$/rGO (10%) catalyst.

Table-2 illustrates the catalytic efficiencies of MB and MG with previously reported photocatalysts. In this investigation, using a 30 mg dosage of the catalyst for 120 min, the $NiFe_2O_4$/rGO (10%) photocatalyst demonstrated an exceptional degradation efficiency (MB-98.01% and MG-98.53%) under visible light irradiation. This is significantly higher than the degradation efficiency of the other reported photocatalysts. Therefore, $NiFe_2O_4$/rGO (10%) photocatalyst would be a better material for environmental remediation.

Recycling studies: A recycling experiment was performed to evaluate the reusability and photostability of the $NiFe_2O_4$/rGO (10%) heterojunction as a photocatalyst [71]. As shown in Fig. 12, the heterojunction retained a high photocatalytic degradation efficiency of 92.70% for MB after five consecutive cycles. The XRD patterns recorded before and after the recycling experiment (Fig. 12b) exhibited comparable diffraction features, with no appreciable changes in the crystalline structure of the reused $NiFe_2O_4$/rGO (10%) compared with the fresh material. The retention of its structural characteristics after repeated use indicates good photostability and durability of the heterojunction. These results support the potential of $NiFe_2O_4$/rGO (10%) for repeated application in photocatalytic dye degradation.

Total organic carbon (TOC) analysis: The total mineralization of MB and MG dyes during photocatalytic degradation by $NiFe_2O_4$/rGO (10%) was evaluated using TOC analysis. TOC measurements provide an estimate of the extent to which organic dye molecules are converted into inorganic carbon species during photocatalytic treatment [72]. Water samples containing MB and MG dyes were analyzed before and after photodegradation in the presence of $NiFe_2O_4$/rGO (10%) and the corresponding TOC results are shown in Fig. 13.

The % TOC removal was calculated using eqn. 3 [73].

$$\text{TOC removal} = \frac{TOC_{before} - TOC_{after}}{TOC_{before}} \times 100 \quad (3)$$

herein, TOC_{before} is the TOC before photodegradation and TOC_{after} is the TOC after photodegradation of MB and MG using $NiFe_2O_4$/rGO (10%). The obtained results revealed that in presence of light, $NiFe_2O_4$/rGO (10%) causes 77.9% and 80.4% mineralization of MB and MG within 120 min. The high TOC removal % after treatment suggests substantial mineralization efficiency of the synthesized catalyst against MG dye [74].

Radical scavenging experiment: Identifying the main active species involved in the degradation process is also crucial to comprehend the photocatalytic mechanism. The reactive species involved in the photocatalytic degradation process were investigated through radical-scavenging experiments using isopropanol (IPA) as a hydroxyl radical ($^{\bullet}OH$) scavenger, disodium ethylenediaminetetraacetate (2Na-EDTA) as a hole (h^+) scavenger and benzoquinone (BQ) as a superoxide radical ($O_2^{\bullet-}$) scavenger [57,75,76]. The corresponding results are shown in Fig. 14. The degradation efficiencies in the presence of IPA, BQ and 2Na-EDTA were 58.60%, 42.85% and 34.61%, respectively. The pronounced decrease in degradation efficiency upon addition of IPA and BQ suggests that $^{\bullet}OH$ and $O_2^{\bullet-}$ radicals are the principal reactive species involved in the MB degradation. The comparatively smaller effect observed with 2Na-EDTA indicates a less prominent contribution of photogenerated holes (h^+) to the degradation process.

Plausible photodegradation mechanism: Fig. 15 proposed the photocatalytic degradation mechanism of the $NiFe_2O_4$/rGO (10%) heterojunction based on the experimental

TABLE-2
COMPARISON OF REPORTED PHOTOCATALYSTS FOR THE DEGRADATION OF MB AND MG UNDER VARIOUS EXPERIMENTAL CONDITIONS

Photocatalyst	Organic pollutant	Light source	Concentration (mg L^{-1}) of MB	Catalyst dose (mg)	Degradation time (min)	Degradation efficiency (%)	Ref.
$NiFe_2O_4$/rGO (10%)	MB/MG	UV-visible light	10	30	120	98.01/98.53	Present work
Cds-$NiFe_2O_4$/rGO	MB	visible light	5-20	5	120	91.40	[64]
Sm-TiO_2/g-C_3N_4	MB	visible light	1	40	120	91.80	[65]
CD @OHCu	MB	UV light	–	–	180	88.20	[66]
$CoFe_2O_4$/g-C_3N_4	MB	visible light	2	200	180	88.00	[67]
TiO_2	MB	visible light	20	30	120	65.00	[68]
$ZnVFe_2O$	MG	visible light	25	–	180	98.00	[69]
TiAgZnO	MG	visible light	5	10	120	70.96	[70]

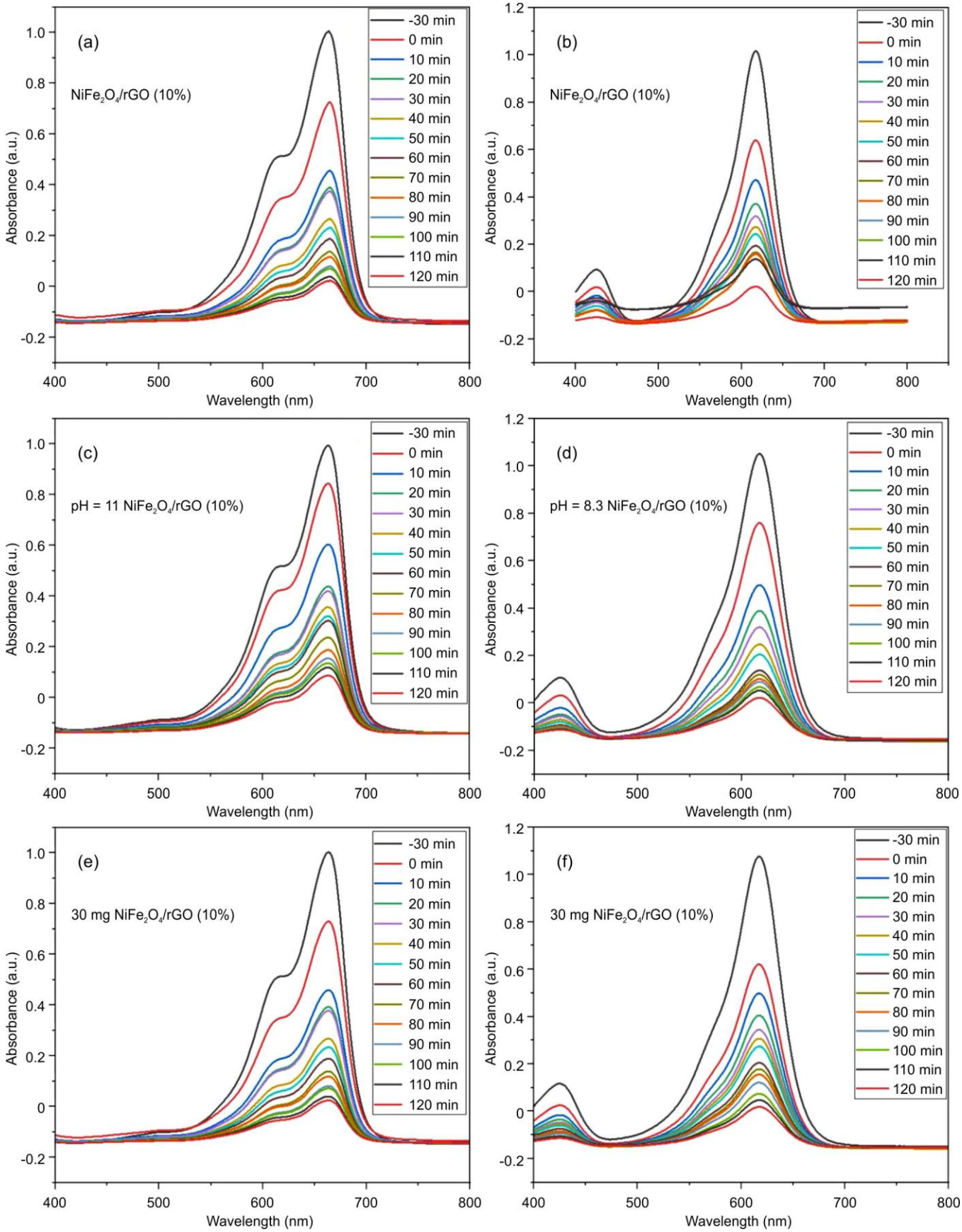

Fig. 11. UV-visible spectra of the $NiFe_2O_4$/rGO (10%) catalyst (a,b), UV-visible spectra of the concentration of the $NiFe_2O_4$/rGO (10%) catalyst (c,d) and UV-visible spectra of the pH of $NiFe_2O_4$/rGO (10%) catalyst (e,f) for MB and MG degradation

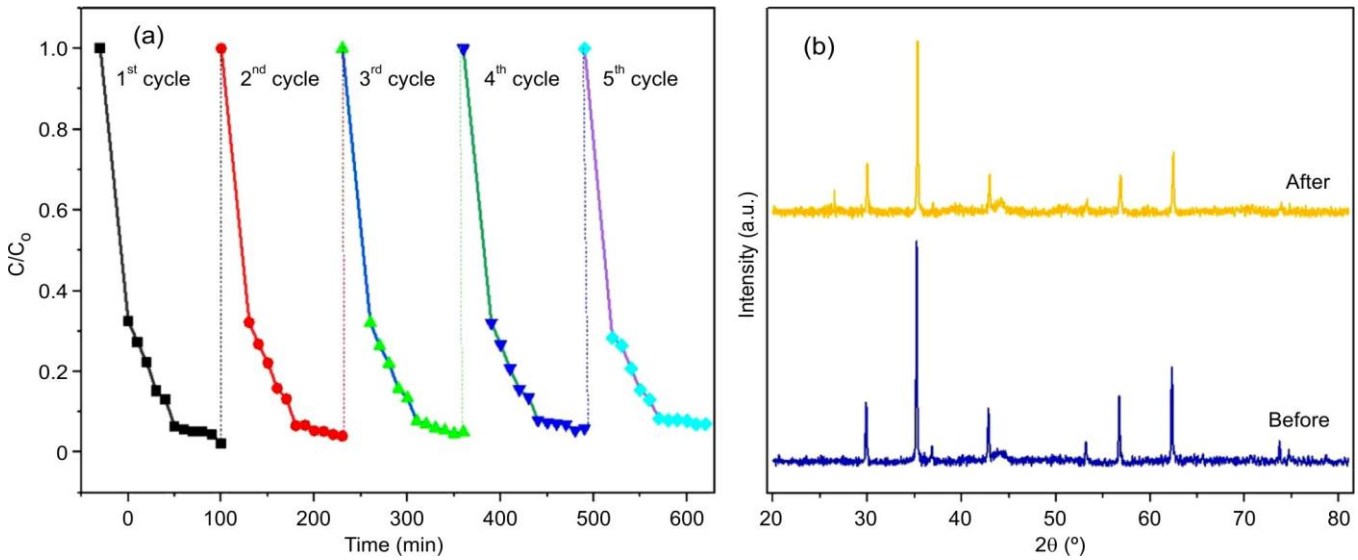

Fig. 12. Recycling performance of $NiFe_2O_4$/rGO (10%) for MB degradation (a) and XRD patterns of the reused catalyst (b)

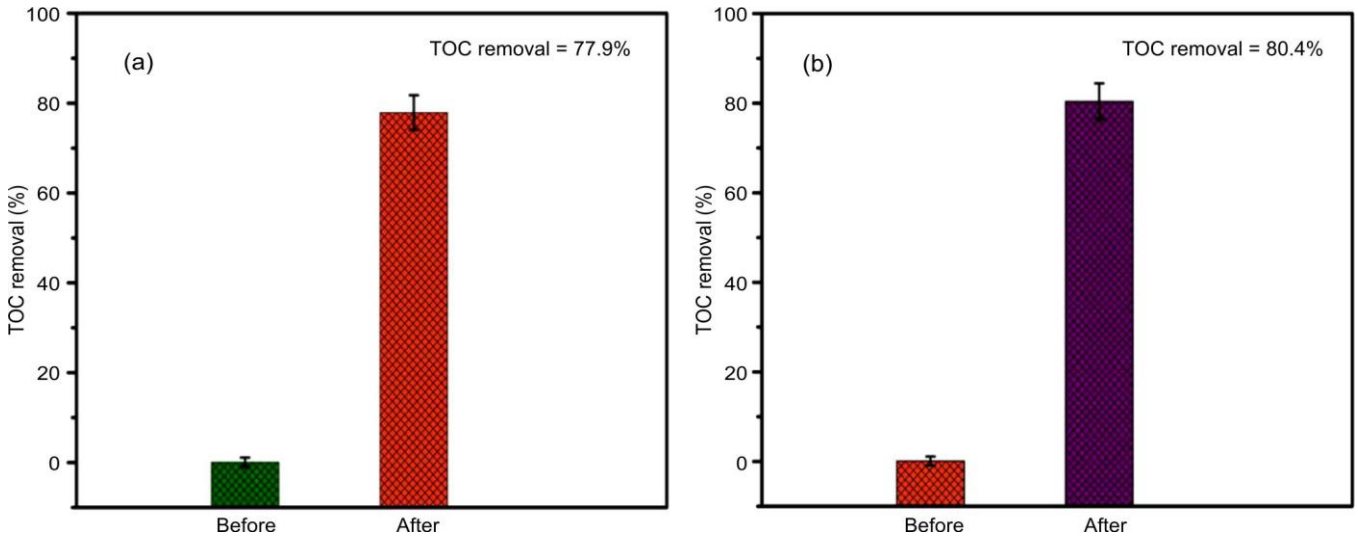

Fig. 13. Total organic carbon removal before and after photocatalytic degradation of (a) MB and (b) MG

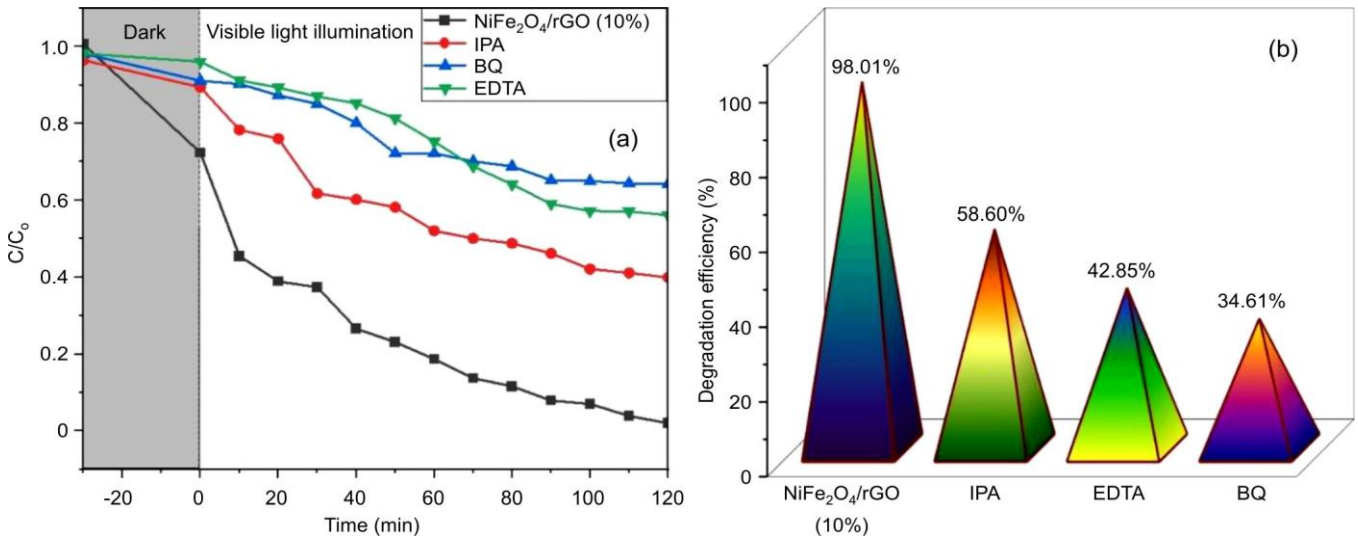

Fig. 14. Photodegradation efficiency of $NiFe_2O_4$/rGO (10%) using IPA, 2-Na EDTA, and BQ scavengers; (b) MB degradation using optimized $NiFe_2O_4$ (10%) catalyst

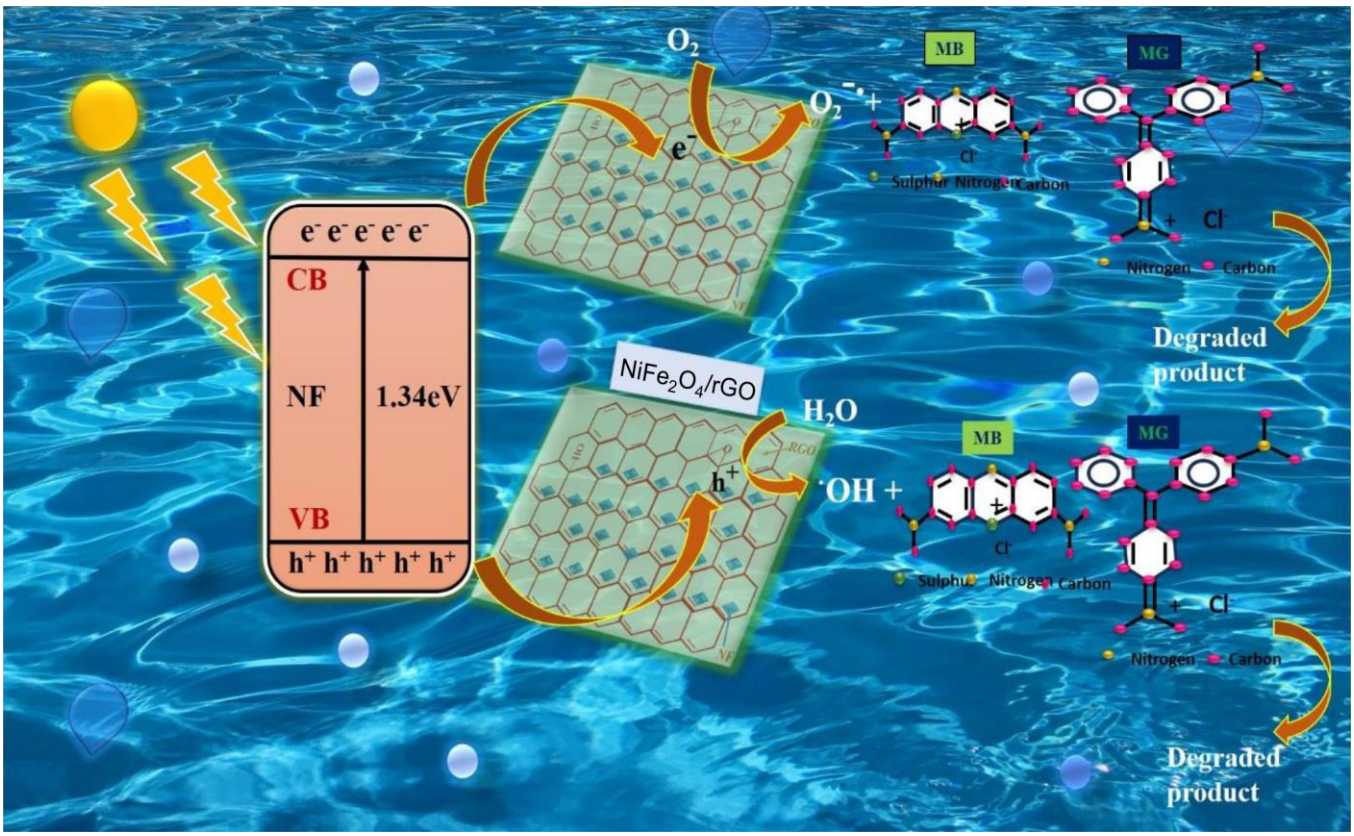

Fig. 15. Plausible photodegradation of MB and MG dye using $NiFe_2O_4$/rGO (10%) catalyst

results. Upon irradiation, the photocatalyst absorbs light energy, promoting electrons (e^-) from the valence band (VB) to the conduction band (CB) and generating corresponding holes (h^+) in the VB. The photoexcited electrons react with dissolved oxygen to form superoxide anion radicals ($O_2^{\bullet-}$), while the photogenerated holes interact with surface hydroxyl groups or water molecules to generate hydroxyl radicals ($^\bullet OH$). These reactive oxygen species attack the dye molecules through successive oxidation reactions, leading to the breakdown of the chromophoric structure and progressive conversion of the organic intermediates into less harmful products, ultimately including CO_2 and H_2O. The proposed pathway in Fig. 15 presents the probable sequence of reactions involved in the photodegradation of the investigated dyes over the $NiFe_2O_4$/rGO (10%) photocatalyst:

$$NiFe_2O_4/rGO + h\nu \longrightarrow NiFe_2O_4/rGO\ [e^-(CB) + h^+(VB)]$$

$$NiFe_2O_4/rGO\ (e^- \text{ in CB}) + \text{Dissolved } O_2 \longrightarrow NiFe_2O_4/rGO + O_2^{\bullet-}\ (\text{superoxide radical})\ [\text{Oxidation}]$$

$$NiFe_2O_4/rGO\ (h^+ \text{ in VB}) + \text{Adsorbed } H_2O \longrightarrow NiFe_2O_4/rGO + {}^\bullet OH\ (\text{hydroxyl radical})\ [\text{Reduction}]$$

$$\text{Dye molecules} + O_2^{\bullet-}/{}^\bullet OH/h^+ \longrightarrow \text{Photodegradation products}$$

Antibacterial activity: Multidrug-resistant *S. aureus* and *E. coli* are important food- and water-borne pathogens, and the antibacterial activity of the synthesized $NiFe_2O_4$/rGO heterojunction is shown in Table-3 [77,78]. $NiFe_2O_4$/rGO exhibited the inhibition zones of 13.03 ± 0.25 mm against Gram-positive *S. aureus* (NCIM 2654) and 11.10 ± 0.26 mm against Gram-negative *E. coli* (NCIM 2256), compared with the control. The MIC values were 100 and 200 mg/mL, respectively. The antibacterial response of $NiFe_2O_4$/rGO differed from that of $NiFe_2O_4$, which may be related to differences in particle size, surface morphology and composition [33]. The stronger response observed against *S. aureus* than *E. coli* can be related to differences in their cell-wall structures, which influence the interaction of nanoparticles with the bacterial surface [79].

The antibacterial effect of $NiFe_2O_4$/rGO is likely associated with more than one mechanism. Contact between the material and bacterial cells can promote the formation of ROS, which can damage cellular components. The release of

TABLE-3
ZONES OF INHIBITION AND MINIMUM INHIBITORY CONCENTRATION (MIC) OF $NiFe_2O_4$ and $NiFe_2O_4$/rGO AGAINST MULTIDRUG-RESISTANT *S. aureus* (NCIM 2654) AND *E. coli* (NCIM 2256)

Samples	Zones of inhibition (mm)		MIC (mg/mL)	
	S. aureus (NCIM 2654)	*E. coli* (NCIM 2256)	*S. aureus* (NCIM 2654)	*E. coli* (NCIM 2256)
$NiFe_2O_4$	17.00 ± 0.20	8.13 ± 0.15	> 400	> 400
$NiFe_2O_4$/rGO	13.03 ± 0.25	11.10 ± 0.26	100	200

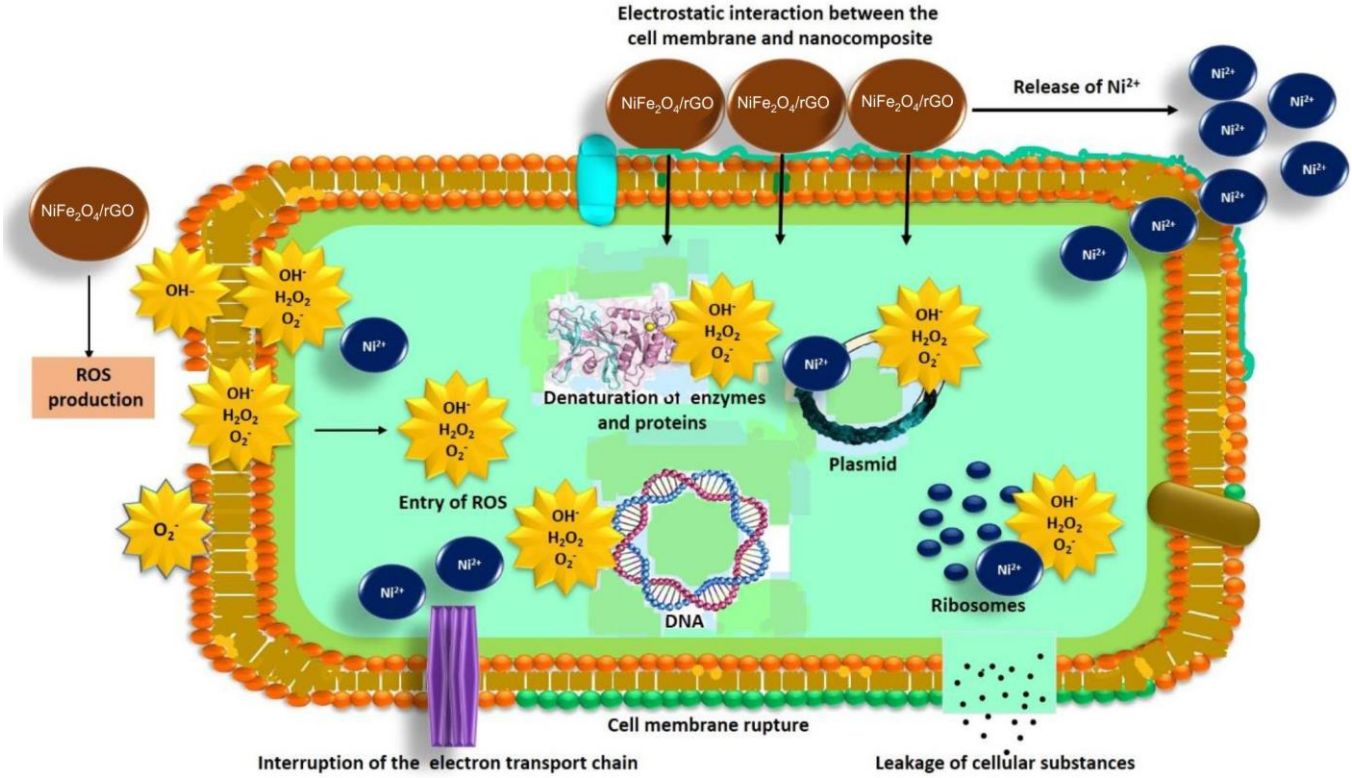

Fig. 16. Plausible mechanism of antibacterial activity of synthesized samples

Ni^{2+} ions may further affect the negatively charged bacterial membrane and disturb membrane-associated proteins [80]. Direct contact of the nanoparticles with the cell surface may cause additional membrane damage through electrostatic interactions and surface-mediated effects. Small particles may interact closely with or penetrate into, the bacterial membrane, leading to leakage of intracellular contents and loss of cell integrity [81,82]. The proposed mechanism for the antibacterial action of the $NiFe_2O_4$/rGO heterojunction is illustrated in Fig. 16.

Conclusion

The synthesis of the $NiFe_2O_4$/rGO heterojunctions was successfully accomplished through a one-pot hydrothermal method. $NiFe_2O_4$/rGO exhibited an octahedron-and hexagon-like morphology with some agglomerated regions. Furthermore, the nickel and iron elements in $NiFe_2O_4$/rGO heterojunction showed +2 and +3 oxidation states. Moreover, the synthesized catalyst exhibited a reduced band gap energy (E_g = 1.34 eV) compared to pure $NiFe_2O_4$. $NiFe_2O_4$/rGO (10%) showed an excellent photocatalytic degradation efficacy for methylene blue (MB) and malachite green (MG) dyes. The optimal conditions for MB removal included a pH of 11 and a catalyst concentration of 30 mg with an illumination time of 120 min. Similarly, for MG removal, optimal conditions were achieved at a pH of 8.3, a catalyst concentration of 30 mg and an illumination time of 120 min. The photocatalytic degradation efficiency was decreased with increasing initial dye concentrations. The pseudo-first-order kinetic model validated the kinetics of MB and MG dyes degradation by $NiFe_2O_4$/rGO (10%), with the rate constant for MB dye degradation being higher than that for MG dye. Furthermore, $NiFe_2O_4$/rGO (10%) heterojunction maintained stable photocatalytic activity even after five reuse cycles. The $NiFe_2O_4$/rGO (10%) heterojunction exhibited considerable antibacterial efficacy against both *S. aureus* and *E. coli* bacterial cells. Depending on the bacterial strain, the antibacterial efficacy got altered, for pristine $NiFe_2O_4$ a larger inhibition zone was observed against *S. aureus*, whereas for the $NiFe_2O_4$/rGO (10%) composite better antibacterial efficacy was displayed against the *E. coli* strain and lower MIC values.

CONFLICT OF INTEREST

The authors declare that there is no conflict of interests regarding the publication of this article.

DECLARATION OF AI-ASSISTED TECHNOLOGIES

During the preparation of this manuscript, the authors used an AI-assisted tool(s) to improve the language and no data, results or scientific conclusions were generated by AI. All analyses, interpretations and conclusions are the authors' own. The authors reviewed and edited the content and take full responsibility for the published work.

REFERENCES

1. J. Hubeny, M. Harnisz, E. Korzeniewska, M. Buta, W. Zielinski, D. Rolbiecki, J. Giebultowicz, G. Nalecz-Jawecki and G. Plaza, *PLoS One*, **16**, e0252691 (2021); https://doi.org/10.1371/journal.pone.0252691
2. A. Periyasamy, *Sustainability*, **16**, 495 (2024); https://doi.org/10.3390/su16020495

3. S. Agustin, A. Kusdiana, W. Rahmah, H. Rusli and G. Kadja, *J. Nanopart. Res.*, **26**, 94 (2024); https://doi.org/10.1007/s11051-024-05996-3
4. S. Gad, V. Murade, S. Nadaf, D. Hase, P. Salve, M. Kalaskar, M. Ayyanar, M. Saoji, N. Gurav and S. Gurav, *Int. J. Biol. Macromol.*, **322**, 146951 (2025); https://doi.org/10.1016/j.ijbiomac.2025.146951
5. K. Obaideen, N. Shehata, E. Sayed, M. Abdelkareem, M. Mahmoud and A. Olabi, *Energy Nexus*, **7**, 100112 (2022); https://doi.org/10.1016/j.nexus.2022.100112
6. E. Ateia and Y. Saeid, *J. Inorg. Organomet. Polym. Mater.*, **34**, 118 (2024); https://doi.org/10.1007/s10904-023-02799-2
7. A. Alsukaibi, *Processes*, **10**, 1968 (2022); https://doi.org/10.3390/pr10101968
8. M. Tiwari and G. Joshi, *J. Sol-Gel Sci. Technol.*, **115**, 1096 (2025); https://doi.org/10.1007/s10971-024-06315-x
9. S. Musmade, D. Hase, A. Waghmare, K. Kadam, A. Gadhave, K. Bhavsar and V. Murade, *J. Water Environ. Nanotechnol.*, **8**, 406 (2023); https://doi.org/10.22090/jwent.2023.04.007
10. S. Patel, D. Hase, K. Bhavsar and V. Murade, *J. Water Environ. Nanotechnol.*, **10**, 141 (2025); https://doi.org/10.22090/jwent.2025.02.003
11. I. Salahshoori, M. Namayandeh Jorabchi, S. Ghasemi, S.M.S. Mirnezami, M.A.L. Nobre and H.A. Khonakdar, *J. Water Process Eng.*, **55**, 104081 (2023); https://doi.org/10.1016/j.jwpe.2023.104081
12. G. Delpiano, D. Tocco, L. Medda, E. Magner and A. Salis, *Int. J. Mol. Sci.*, **22**, 788 (2021); https://doi.org/10.3390/ijms22020788
13. M. Mohammadnejad, N. Nekoo, S. Alizadeh, S. Geranmayeh and S. Sadeghi, *Sci. Rep.*, **13**, 17981 (2023); https://doi.org/10.1038/s41598-023-45075-6
14. N. Al-Kadhi, E. Abdelrahman, F. Alamro, F. Saad and D. Al-Raimi, *J. Inorg. Organomet. Polym. Mater.*, **35**, 5092 (2025); https://doi.org/10.1007/s10904-024-03577-4
15. J. Xu, T. Wang, M. Wei, Y. Yang, D. Li, H. Yu and X. Dong, *J. Ind. Eng. Chem.*, **136**, 615 (2024); https://doi.org/10.1016/j.jiec.2024.02.050
16. S. Jaafar, R. Faeq, A. Naji, O. Nief and M. Mohammed, *RSC Adv.*, **14**, 26066 (2024); https://doi.org/10.1039/D4RA05096G
17. I.G. Diniz Dias de Azevedo, M.A. Morales Torres, C. Pereira de Souza and A.L. Lopes Moriyama, *Catalysts*, **14**, 73 (2024); https://doi.org/10.3390/catal14010073
18. J. Navarro, C. Hurtado, M. Gonzalez-Castano, L. Bobadilla, S. Ivanova, F. Cumbrera, M. Centeno and J. Odriozola, *J. CO2 Util.*, **68**, 102356 (2023); https://doi.org/10.1016/j.jcou.2022.102356
19. R. Chang, C. Ding, H. Long, X. Lv, T. Chun, C. Peng, R. Wei, X. Xu, Z. Yan, Y. Sun, X. Wang, S. Xue and W. Lv, *J. Colloid Interface Sci.*, **682**, 353 (2025); https://doi.org/10.1016/j.jcis.2024.11.201
20. F. Mirshafiee and M. Rezaei, *Sci. Rep.*, **14**, 20818 (2024); https://doi.org/10.1038/s41598-024-71501-4
21. A. Soufi, H. Hajjaoui, R. Elmoubarki, M. Abdennouri, S. Qourzal and N. Barka, *Appl. Surf. Sci. Adv.*, **6**, 100145 (2021); https://doi.org/10.1016/j.apsadv.2021.100145
22. S. Salih and W. Mahmood, *Heliyon*, **9**, e16601 (2023); https://doi.org/10.1016/j.heliyon.2023.e16601
23. S. Musmade, D. Hase, K. Kadam, G. Pandhare, K. Bhavsar, M. Khan, M. Khan, S. Gurav and V. Murade, *J. Inorg. Organomet. Polym. Mater.*, **35**, 1708 (2025); https://doi.org/10.1007/s10904-024-03389-6
24. A. Mondal, A. Prabhakaran, S. Gupta and V. Subramanian, *ACS Omega*, **6**, 8734 (2021); https://doi.org/10.1021/acsomega.0c06045
25. M. Ahmed and A. Mohamed, *RSC Adv.*, **13**, 421 (2022); https://doi.org/10.1039/D2RA07225D
26. V. Murade, S. Darandale and D. Hase, *J. Water Environ. Nanotechnol.*, **11**, 144 (2026); https://doi.org/10.22090/jwent.2026.01.10
27. K. Rana, H. Kaur, N. Singh, T. Sithole and S. Siwal, *Next Mater.*, **3**, 100107 (2024); https://doi.org/10.1016/j.nxmate.2024.100107
28. M. Mohammed, A. Naji, D. Ahmed, M. Jamai, M. Dehghanipour, E. Salih, S. Bhattarai, R. Pandey, J. Madan and M. Rahman, *J. Sol-Gel Sci. Technol.*, **115**, 1145 (2025); https://doi.org/10.1007/s10971-024-06619-y
29. Q. Wu and Y. Song, *Water Sci. Technol.*, **87**, 1465 (2023); https://doi.org/10.2166/wst.2023.077
30. Z. Iqbal, M. Tanweer and M. Alam, *ACS Omega*, **8**, 6376 (2023); https://doi.org/10.1021/acsomega.2c06636
31. J. Sin, S. Lam, H. Zeng, H. Lin, H. Li, L. Huang, A. Mohamed, K. Tham, and J. Lim, *Environ. Res.*, **212**, 113394 (2022); https://doi.org/10.1016/j.envres.2022.113394
32. Y. Yao, Z. Yang, D. Zhang, W. Peng, H. Sun and S. Wang, *Ind. Eng. Chem. Res.*, **51**, 6044 (2012); https://doi.org/10.1021/ie300271p
33. N. Arumugham, A. Mariappan, J. Eswaran, R. Kanthapazham, S. Daniel and P. Kathirvel, *J. Hazard. Mater. Adv.*, **8**, 100156 (2022); https://doi.org/10.1016/j.hazadv.2022.100156
34. Y. Zhang and X. Li, *Mater. Res. Bull.*, **197**, 113981 (2026); https://doi.org/10.1016/j.materresbull.2025.113981
35. B. Palanivel and M. Alagiri, *ChemistrySelect*, **5**, 9765 (2020); https://doi.org/10.1002/slct.202002519
36. W. Shen, L. Zhang, B. Zhao, Y. Du and X. Zhou, *Ceram. Int.*, **44**, 9809 (2018); https://doi.org/10.1016/j.ceramint.2018.02.219
37. N. Malesic-Eleftheriadou, E. Evgenidou, G. Kyzas, D. Bikiaris and D. Lambropoulou, *Chemosphere*, **234**, 746 (2019); https://doi.org/10.1016/j.chemosphere.2019.05.239
38. P. Mahamuni-Badiger, P. Patil, M. Badiger, P. Patel, B. Thorat-Gadgil, A. Pandit and R. Bohara, *Mater. Sci. Eng. C*, **108**, 110319 (2020); https://doi.org/10.1016/j.msec.2019.110319
39. P. Mahamuni, P. Patil, M. Dhanavade, M. Badiger, P. Shadija, A. Lokhande and R. Bohara, *Biochem. Biophys. Rep.*, **17**, 71 (2019); https://doi.org/10.1016/j.bbrep.2018.11.007
40. P. Mahamuni-Badiger, P. Patil, P. Patel, M. Dhanavade, M. Badiger, Y. Marathe and R. Bohara, *New J. Chem.*, **44**, 9754 (2020); https://doi.org/10.1039/D0NJ01384F
41. S. Shokri, N. Shariatifar, E. Molaee-Aghaee, G. Khaniki, P. Sadighara, M. Faramarzi, M. Mohammadi and A. Rezagholizade-Shirvan, *Sci. Rep.*, **13**, 15777 (2023); https://doi.org/10.1038/s41598-023-42974-6
42. L. Yao, Y. Wang, J. Zhao, Y. Zhu and M. Cao, *Small*, **19**, e2208101 (2023); https://doi.org/10.1002/smll.202208101
43. Z. Alaizeri, H. Alhadlaq, S. Aldawood, M. Javed Akhtar and M. Ahamed, *Saudi Pharm. J.*, **31**, 101735 (2023); https://doi.org/10.1016/j.jsps.2023.101735
44. S. Divya, P. Sivaprakash, S. Raja, S. Muthu, E. Eed, S. Arumugam and T. Oh, *Appl. Nanosci.*, **13**, 1327 (2023); https://doi.org/10.1007/s13204-021-02026-9
45. N. Esther, V. Judith, B. Al-Najar, L. Hazeem, M. Bououdina, K. John, K. Kombaiah and S. Bellucci, *Bioinorg. Chem. Appl.*, **2022**, 805490 (2022); https://doi.org/10.1155/2022/4805490
46. N. Askari, N. Salarizadeh and M. Askari, *J. Mater. Sci. Mater. Electron.*, **32**, 9765 (2021); https://doi.org/10.1007/s10854-021-05636-9
47. S. Rana, S. Basu and C. Mukhopadhyay, *Mol. Divers.*, **26**, 2561 (2022); https://doi.org/10.1007/s11030-021-10356-7
48. Z. Yuan, Z. Chen, D. Chen and Z. Kang, *Ultrason. Sonochem.*, **22**, 188 (2015); https://doi.org/10.1016/j.ultsonch.2014.07.009
49. Renu, Komal, R. Kaur, J. Kaur, Jyoti, V. Kumar, K.B. Tikoo, S. Rana, A. Kaushik and S. Singhal, *J. Electroanal. Chem.*, **887**, 115161 (2021); https://doi.org/10.1016/j.jelechem.2021.115161
50. P. Shinde, C. Rout, D. Late, P. Tyagi and M. Singh, *Int. J. Hydrogen Energy*, **46**, 2617 (2021); https://doi.org/10.1016/j.ijhydene.2020.10.144
51. B. Palanivel, C. Ayappan, V. Jayaraman, S. Chidambaram, A. Mani and R. Maheswaran, *Mater. Sci. Semicond. Process.*, **100**, 87 (2019); https://doi.org/10.1016/j.mssp.2019.04.040
52. N. Dalai, B. Mohanty, A. Mitra and B. Jena, *ChemistrySelect*, **4**, 7791 (2019); https://doi.org/10.1002/slct.201901465

53. S. Kapoor, V. Kumar, K. Tikoo, B. Chudasama, N. Goel and S. Singhal, *Ceram. Int.*, **46**, 2724 (2020); https://doi.org/10.1016/j.ceramint.2019.09.262
54. A. Behera, A.K. Kar and R. Srivastava, *Inorg. Chem.*, **61**, 12781 (2022); https://doi.org/10.1021/acs.inorgchem.2c01899
55. T. Pajkossy, M.U. Ceblin and G. Mészáros, *J. Electroanal. Chem.*, **899**, 115655 (2021); https://doi.org/10.1016/j.jelechem.2021.115655
56. Y. Mao, J. Zhang, Y. Zhao, X. Wei, D. Jiang, L. Zhu, Y. Asakura, Q.M. Phung, H.N. Nam, H.-Y. Hsu and Y. Yamauchi, *J. Colloid Interface Sci.*, **694**, 137614 (2025); https://doi.org/10.1016/j.jcis.2025.137614
57. H. Xi, H. Wang, D. Liu, Q. Mu, X. Xu, Q. Kang, Y. Yang, Z. Yang and Z. Lei, *J. Alloys Compd.*, **1010**, 177818 (2025); https://doi.org/10.1016/j.jallcom.2024.177818
58. P. Agboola and I. Shakir, *J. Korean Ceram. Soc.*, **59**, 686 (2022); https://doi.org/10.1007/s43207-022-00209-w
59. X. Li, Y. Chen, Y. Tao, L. Shen, Z. Xu, Z. Bian and H. Li, *Chem Catal.*, **2**, 1315 (2022); https://doi.org/10.1016/j.checat.2022.04.007
60. M. Tamilchezhiyan, A. Begum, M. Parthibavarman and S. Aravindan, *Diamond Rel. Mater.*, **151**, 111817 (2025); https://doi.org/10.1016/j.diamond.2024.111817
61. A. Alakshar, M. Goher, M. Abd El-Moghny and M. El-Deab, *Desalination Water Treat.*, **320**, 100676 (2024); https://doi.org/10.1016/j.dwt.2024.100676
62. T. Ramasamy, L. Satheesh, V. Selvaraj, O. Bazaka, I. Levchenko, K. Bazaka and M. Mandhakini, *Nanomaterials*, **12**, 3822 (2022); https://doi.org/10.3390/nano12213822
63. S. Goktas, *Chem. Afr.*, **7**, 4425 (2024); https://doi.org/10.1007/s42250-024-01036-8
64. M. Bagherzadeh, R. Kaveh, S. Ozkar and S. Akbayrak, *Res. Chem. Intermed.*, **44**, 5953 (2018); https://doi.org/10.1007/s11164-018-3466-1
65. T. Cui, Y. Zhang, Y. Yan, J. Zhao, K. Qi and J. Jiang, *Appl. Organomet. Chem.*, **36**, e6626 (2022); https://doi.org/10.1002/aoc.6626
66. M. Cui, J. Jiang, Z. Song and T. Ren, *Inorg. Chem. Commun.*, **158**, 111559 (2023); https://doi.org/10.1016/j.inoche.2023.111559
67. A. Ajami, S. Sheibani and A. Ataie, *J. Mater. Res. Technol.*, **30**, 2168 (2024); https://doi.org/10.1016/j.jmrt.2024.04.010
68. D. Bopape, Z. Tetana, N. Mabuba, D. Motaung and N. Hintsho-Mbita, *Results Chem.*, **5**, 100825 (2023); https://doi.org/10.1016/j.rechem.2023.100825
69. E. Mostafa and E. Amdeha, *Environ. Sci. Pollut. Res. Int.*, **29**, 69861 (2022); https://doi.org/10.1007/s11356-022-20745-6
70. S. Kerli, M. Kavgaci, A. Soguksu and B. Avar, *Braz. J. Phys.*, **52**, 22 (2022); https://doi.org/10.1007/s13538-021-01007-1
71. K. Chitalkar, D. Hase, S. Gurav, S. Musmade, R. Gaikar, M. Sillanpaa, V. Murade and H. Aher, *J. Inorg. Organomet. Polym. Mater.*, **35**, 6961 (2025); https://doi.org/10.1007/s10904-025-03705-8
72. K.-H. Nguyen, T.-H. Le, T.-D. To, X.-D. Nghiem and D.T. Tran, *Diamond Rel. Mater.*, **161**, 113091 (2026); https://doi.org/10.1016/j.diamond.2025.113091
73. I. Jamil, A. Alasiri, F. Nawaz, M. Rashid, A.A. Elfar and M.E. Hoque, *Nanomaterials*, **16**, 721 (2026); https://doi.org/10.3390/nano16120721
74. L. Mohanty, D. Sundar Pattanayak, R. Singhal, D. Pradhan and S. Kumar Dash, *Inorg. Chem. Commun.*, **138**, 109286 (2022); https://doi.org/10.1016/j.inoche.2022.109286
75. K. Bhavsar, P. Labhane, V. Murade and G. Sonawane, *Inorg. Chem. Commun.*, **160**, 111901 (2024); https://doi.org/10.1016/j.inoche.2023.111901
76. K. Bhavsar, P. Labhane, V.D. Murade, R.B. Dhake and G.H. Sonawane, *Inorg. Chem. Commun.*, **133**, 108958 (2021); https://doi.org/10.1016/j.inoche.2021.108958
77. S. Kumar, R. Mahato, S. Ch and S. Kumbham, *Microbe*, **6**, 100281 (2025); https://doi.org/10.1016/j.microb.2025.100281
78. W. Albuquerque, A. Macrae, O. Sousa, G. Vieira and R. Vieira, *Braz. J. Microbiol.*, **38**, 131 (2007); https://doi.org/10.1590/S1517-83822007000100027
79. A. Rahman, S. Zulfiqar, A. Haq, I. Alsafari, U. Qazi, M. Warsi and M. Shahid, *Ceram. Int.*, **47**, 9513 (2021); https://doi.org/10.1016/j.ceramint.2020.12.085
80. Y. Baek and Y. An, *Sci. Total Environ.*, **409**, 1603 (2011); https://doi.org/10.1016/j.scitotenv.2011.01.014
81. K. Rincon-Granados, A. Vazquez-Olmos, A. Rodriguez-Hernandez, A. Vega-Jimenez, F. Ruiz, V. Garibay-Febles and L. Ximenez-Fyvie, *Materialia*, **15**, 100955 (2021); https://doi.org/10.1016/j.mtla.2020.100955
82. K. Lingaraju, H. Raja Naika, H. Nagabhushana, K. Jayanna, S. Devaraja and G. Nagaraju, *Arab. J. Chem.*, **13**, 4712 (2020); https://doi.org/10.1016/j.arabjc.2019.11.003